Achieving consistency between in-situ and remotely sensed optical and microphysical properties of Arctic cirrus: the impact of far-infrared radiances

Gianluca Di Natale[1], Helen Brindley[2], Laura Warwick[3], Sanjeevani Panditharatne[2,4], Ping Yang[5], Robert Oscar David[6], Tim Carlsen[6], Sorin Nicolae Vâjâiac[7], Alex Vlad[7,8], Sorin Ghemulet[7], Richard Bantges[2], Andreas Foth[9], Martin Flügge[10], Reidar Lyngra[10], Hilke Oetjen[3], Dirk Schuettemeyer[3], Luca Palchetti[1], and Jonathan Murray[2]

[1]Consiglio Nazionale delle Ricerche, National Institute of Optics, Via Madonna del Piano, 10, Sesto Fiorentino, 19100, Firence, Italy
[2]Department of Physics and National Centre for Earth Observation, Imperial College, London, UK
[3]ESA/ESTEC, Noordwijk, the Netherlands
[4]RAL Space, Harwell Oxford, Chilton, UK
[5]Department of Atmospheric Sciences, Texas A&M University, CollegeStation, TX 77843, USA
[6]Department of Geosciences, University of Oslo, Oslo, Norway
[7]National Institute for Aerospace Research "Elie Carafoli", Bucharest, Romania
[8]University of Bucharest, Faculty of Physics, 405 Atomistilor, Magurele 077125, Romania
[9]Leipzig University, Leipzig Institute for Meteorology, Leipzig, Germany
[10]Andøya Space, Andøya, Norway

Correspondence: Gianluca Di Natale (gianluca.dinatale@ino.cnr.it)

Abstract. This paper explores whether it is possible to achieve consistency between ground-based infrared radiance measurements made in the presence of cirrus, co-located in-situ aircraft measurements of the cirrus microphysics, and ancillary ground-based remote sensing. Specifically we use spectrally resolved radiances covering the range 400-1500 cm^{-1}, in-situ measurements of cirrus particle sizes and habits, backscatter ceilometer observations of cloud vertical structure and microwave

5   inferred temperature and humidity profiles to investigate whether we can obtain consistency between the derived cloud properties and atmospheric state from these independent sources of data. The primary focus of this study is on the sensitivity of the retrieved cloud particle size to the assumed crystal habit. Excellent consistency between the retrieved cloud parameters is achieved both with the ceilometer derived optical depth and the size distribution measured by the aircraft by assuming the crystal habit to be comprised of bullet rosettes. The averaged values of the effective diameter and optical depth obtained from

10   radiometric measurements are (26.5±1.8) μm and (0.12±0.01) in comparison with the values derived from in-situ and ceilometer measurements equal to (31.5±5.0) μm and (0.13±0.01), respectively. Furthermore, we show that the radiance information contained within the far-infrared (wavenumbers < 650 cm^{-1}) spectrum is critical to achieving this level of agreement with the in-situ aircraft observations. The results emphasize why it is vital to expand the current limited database of measurements encompassing the far-infrared spectrum, particularly in the presence of cirrus, to explore whether this finding holds over a

15   wider range of conditions.

1 Introduction

Cirrus clouds play a vital role in regulating the energy balance of our planet and in determining how it, and hence Earth's climate, may evolve in the future (e.g. Lynch (1996), Dawson and Schiro (2025)). Most studies imply that cirrus imparts a net warming to the climate system (Choi and Ho, 2006) but that the degree of warming is dependent on the cloud fraction, geographical location, altitude, and, crucially, optical thickness. Theoretical considerations and model projections point towards an increase in high cloud altitude in a warming climate (e.g. Hartmann and Larson (2002); Chepfer et al. (2002)), which, in the absence of any other change, would be expected to enhance the associated cloud radiative heating (Gasparini et al., 2024). Conversely, while observational studies of the response to inter-annual surface temperature variability indicate an increase in cirrus amount with warming (Zhou et al., 2014), model studies imply a reduction in the coverage of anvil cirrus with increasing surface temperature via the 'iris-stability' hypothesis (e.g. Bony et al. (2016)). More recent observational studies imply a small tropical high cloud feedback due to compensating longwave and shortwave effects associated with changes in coverage, altitude and optical thickness (Raghuraman et al., 2024). Whatever response is ultimately realised, exactly how changes to cirrus coverage and location manifest radiatively will also critically depend on whether the associated cloud microphysics are also altered.

For example, previous work has shown the substantial impact of changes in particle size distribution on cirrus longwave heating rates, with the presence of smaller particles causing a sizeable increase in heating (e.g. Stackhouse and Stephens (1991)). Similarly, relatively simple parameterisations expressing cloud emittance as a function of effective radius have been used to demonstrate that the particle size of ice crystals determines if the presence of cirrus results in a positive or negative ice-water feedback and, consequently, an additional surface warming or cooling depending on the sign of the feedback (e.g. Stephens et al. (1990)).

A second difficulty in describing the interaction between radiation and cirrus is due to the myriad of different crystal habits which can exist in nature. Each shows different absorption and scattering behavior (Baran, 2009; Baran et al., 2014). Improved knowledge of the crystal habit distribution within cirrus, alongside measures of the crystal size and overall cloud optical depth is therefore critical to reducing uncertainty in their radiative effect.

Finally, to tie cirrus micro-physical and optical properties to their radiative impact we need to have confidence in the tools we use to simulate radiances and fluxes in the presence of these clouds. While a number of observational campaigns have taken place to assess cirrus 'radiative closure' over the visible, mid-infrared and microwave part of the Earth's electromagnetic spectrum (Meyer et al., 2016; Evans et al., 1999; Lawson et al., 2006; Turner and Mlawer, 2010), considerably fewer equivalent studies cover the far-infrared (FIR), typically defined as wavelengths between 15–100 μm . Simulations have long highlighted the dominant contribution that we expect the FIR to make to the Earth's total outgoing longwave radiation and greenhouse effect (Brindley and Harries, 1998; Collins and Mlynczak, 2001), particularly for colder scenes. However, aircraft-based studies which attempt to reconcile FIR radiances measured in the presence of cirrus with simulations struggle to do so, even when using ice optical property databases that are routinely employed in satellite retrievals exploiting the mid-infrared and visible parts of the spectrum (Cox et al., 2007; Bantges et al., 2020), but that are still not validated in the FIR.

Part of the issue with these existing studies may be related to the experimental design. All employed a single aircraft platform, with in-situ sampling of the cloud microphysics necessarily occurring at a different time to the above-cloud radiance measurements. Hence, it is impossible to unambiguously map the cirrus properties to its radiative signature. An alternative to this approach is to use zenith-view radiances measured from the ground in the presence of cirrus. With this set-up, a very dry atmosphere is required to avoid the cirrus radiative signatures in the FIR being obscured by strong absorption by water vapour. Exploiting such conditions, zenith radiances have been used to retrieve ice cloud properties over the Arctic and Antarctica from Extended and Polar Atmospheric Emitted Radiance Interferometers (E-AERI, P-AERI), extending down to 550 and 400 cm^{-1}, respectively, in a number of field campaigns (Maesh et al., 2001a, b; Turner et al., 2003; Garrett and Zhao, 2013; Shupe et al., 2013). Similarly, a multi-year, database of FIR radiances has been collected by the Radiation Explorer in the Far InfraRed - Prototype for Applications and Development (REFIR-PAD), operating autonomously at the Dome-C site Antarctica since 2011 (Palchetti et al., 2015; Bianchini et al., 2019). Several studies have exploited the data, developing methods to characterise cloud type and derive optical depth and size information (Di Natale et al., 2020). Most recently, observations from the Far Infrared Radiation Mobile Observation System (FIRMOS, Belotti et al. (2023)) taken from Zugspitze in the German Alps demonstrated the consistency of optical depth retrievals derived from zenith view infrared radiances with those estimated from simultaneous backscatter ceilometer observations (Di Natale et al., 2021). The development and deployment of FIRMOS was undertaken specifically in preparation for the Far-infrared Outgoing Radiation Understanding and Monitoring (FORUM) Earth Explorer 9 mission (Palchetti et al., 2020).

Despite the notable advances made in these ground-based studies, including the key step of linking observations from complementary sensors to the measured infrared radiances, none include simultaneous in-cloud observations. In this paper we exploit a dataset collected as part of the MC2-ICEPACKS campaign, based at Andøya, Norway during February-March 2023 (David et al, in prep). The data include downwelling radiance observations made by the Far-INfrarEd Spectrometer for Surface Emissivity (FINESSE, Murray et al. (2024)) alongside independent measurements of the atmospheric vertical structure and, uniquely, contemporaneous in-situ sampling of cirrus microphysics from aircraft. We use these data to provide a well-characterised test of our ability to achieve consistency between measured and retrieved atmospheric temperature and water vapour profiles, ozone total columns and cloud optical and micro-physical properties given currently available parameterizations of ice crystals, with a particular emphasis on demonstrating observationally how FIR radiances can constrain crystal habit. This aspect is well known and has been studied in the literature (Di Natale et al., 2024). However, to the best of our knowledge, the capability to achieve a better consistency with one habit distribution compared to another has never been demonstrated. Furthermore, a previous study of the consistency between the optical and microphysical properties of clouds, exploiting spectral radiance measurements in the FIR together with ground-based data such as radar reflectivity and particle imaging, has already been carried out from Antarctica (Di Natale et al., 2022). However, in these studies remotely sensed cloud microphysics (particle size and habit) were only compared with ground-collected measurements of precipitating ice crystals: they have never before been compared with in situ data acquired inside cirrus clouds, as is done in the present work.

Our manuscript is structured as follows: in section 2 we introduce the measurement field campaign and the instruments involved in the experiment; in section 3 we describe the methodology applied through the comparison of the retrieval products

85 with the available measurements and the retrieval method applied; in section 4 we show and discuss the results and in section 5 we demonstrate the improvement in retrieval quality when FIR radiances are available to constrain habit selection. Finally, in section 6 we draw conclusions and outline areas for future work.

2 MC2-ICEPACKS Campaign instrumentation

The Mixed-phase Clouds and Climate -Ice Pockets in Arctic Clouds at sub-Kilometer Scales campaign (MC2-ICEPACKS) took
90 place from 13th February to 17th March 2023, based at Andøya, Norway, with a primary goal of investigating the distribution of Arctic cloud phase in order to improve its representation in Earth System Models (David et al, in prep). The campaign consisted of a ground-based segment and airborne measurements. The ground-based segment was hosted at both the Arctic LiDAR Observatory for Middle Atmosphere Research (ALOMAR) that is located on top of the Ramnan mountain 378 m a.s.l. and at Andøya Space (Fig. 1), located at 12 m a.s.l.. The airborne measurements were facilitated by the National Institute for
95 Aerospace Research of Romania (INCAS) Atmospheric Research Laboratory aircraft that was stationed at Andøya Airport. The horizontal distance between ALOMAR and Andøya Space is approximately 2.1 km.
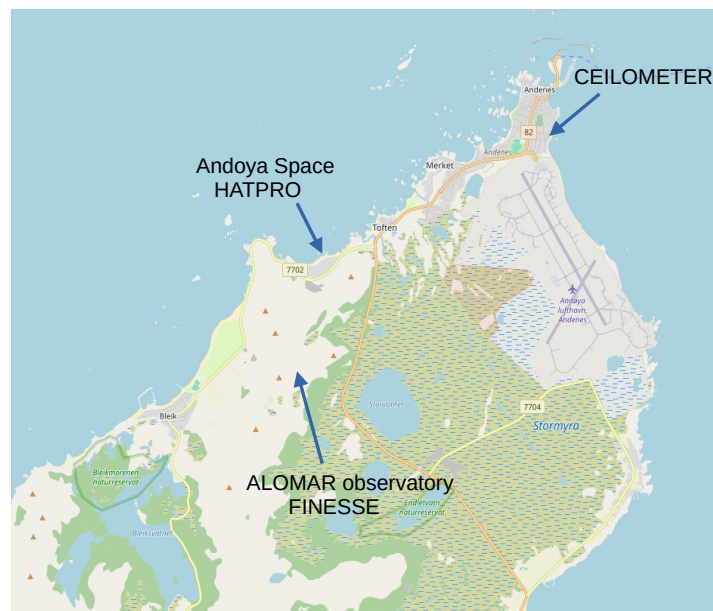
Figure 1. Location of ground-based instrumentation during the MC2-ICEPACKS campaign. FINESSE was located at an elevation of 378 m a.s.l., at ALOMAR [69.28°N, 16.01°E]. The HATPRO was installed at Andøya Space and the ceilometer close to Andenes (0 m a.s.l.). Background map: © OpenStreetMap contributors, data available under the Open Database License (ODbL). Retrieved from www.openstreetmap.org.

This paper concentrates on the measurements conducted on 17th February 2023, when thin, patchy cirrus clouds were observed over ALOMAR. These were sampled by the INCAS aircraft (section 2.1) between 08:15 and 08:45 UTC during

an extended research flight (Fig. 2). Simultaneous ground-based observations were performed by FINESSE (section 2.2), a
ceilometer (section 2.3, see Fig. 1) and a Humidity And Temperature PROfilers (HATPRO) radiometer (section 2.4) located at
Andøya Space.

2.1 INCAS aircraft

The INCAS aircraft, a Hawker Beechcraft King Air C90GTx (INCAS KA), is equipped with two combination cloud probes
mounted under the wings (e.g. Vâjâiac et al. (2021)), namely a HAWKEYE (SPEC, Boulder, CO) and a Cloud, Aerosol and
Precipitation Spectrometer (CAPS; DMT, Boulder, CO)). The HAWKEYE includes a 2D-S, which combines two orthogonally
oriented optical array probes with 10 and 50 µm resolution, respectively (spanning from 10 to 1280 and 50 to 6400 µm), a
cloud particle imager (CPI) that takes 2-D images of cloud particles between 2.3-6400 μm and a Fast Cloud Droplet Probe for
sampling the size distribution of smaller particles, from 1.5-50 μm (e.g., Lawson et al. (2001); Woods et al. (2018)). The CAPS
provides similar aerosol and hydrometeor size information but due to an optical alignment issue during the presented case
study, it was only used for observations of the true air speed, temperature and pressure during the flight. The ice crystal particle
size distributions (PSDs) used here are calculated from the 50 μm -channel of the 2D-S using the System for OAP (optical
array probe) Data Analysis (SODA2; developed at NCAR). During post-processing only ice crystals which were captured
completely within the optical array ('all-in'; Heymsfield and Parrish (1978)) were considered and their size was calculated
using the circle-fit method, or the diameter of the smallest circle that encompasses them (Wu and McFarquhar, 2016). The
influence of shattered particles was removed following Field et al. (2006).
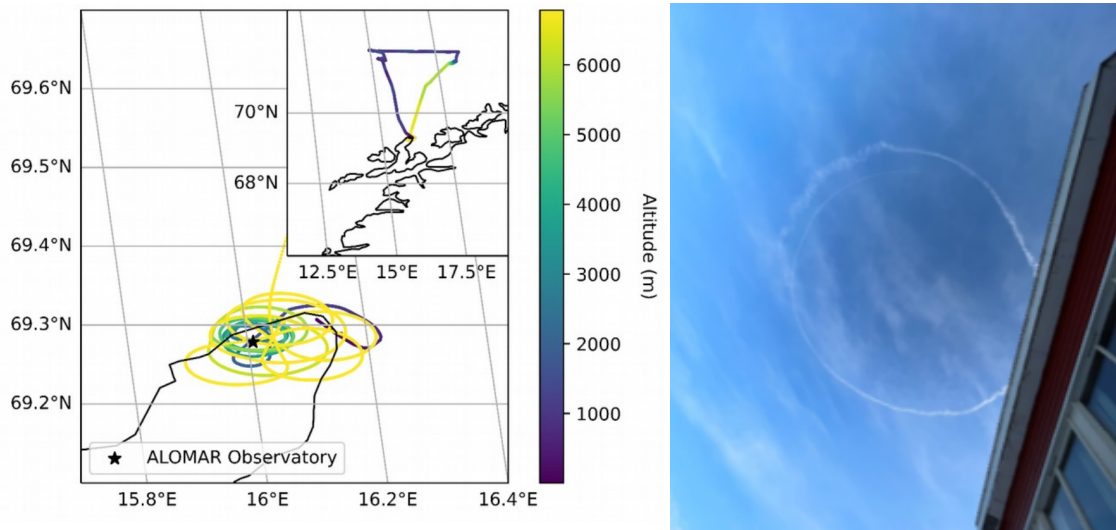
Figure 2. Left: Main image - Flight track of INCAS KA on 17th February 2023 over ALOMAR between 08:00-08:45 UTC. The colour
shows the altitude of the INCAS KA. Inset – Trajectory of the entire science flight. Right: Sky conditions above FINESSE at 08:24 UTC
during the INCAS KA overpass (credit J.Murray)
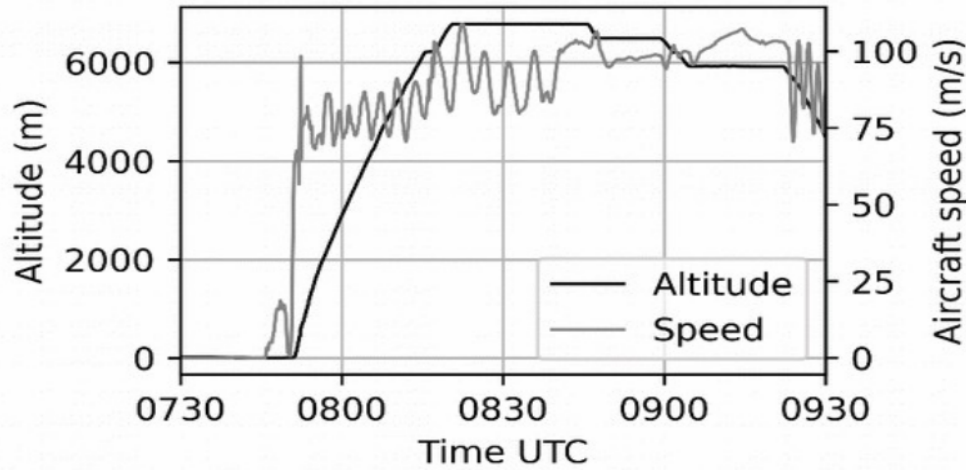
Figure 3. INCAS KA altitude and velocity as a function of time during the February 17th 2023 flight. The INCAS KA was over ALOMAR between approximately 08:15-08:45 UTC as the aircraft contrail was clearly visible from the ground.

On 17th February the INCAS KA made several passes over ALOMAR with the aim of in-situ sampling of the cirrus cloud that was in the field of view (FOV) of FINESSE. The left panel of Fig. 2 shows the trajectory of the aircraft with the colour indicating the altitude of the aircraft. The right panel indicates its location above FINESSE just before the point of closest approach. Fig. 3 shows the variation in aircraft altitude and velocity during the flight with time. The airborne team used visual

120 and near-real time observations from the cloud probes to guide their flight level, implying that the cirrus above ALOMAR was at an altitude between 6-7 km with a peak at approximately 6.7 km.

The FINESSE FOV is about 30 mrad so that the radiance detected by the instrument come from an area of about 180 m at the altitude of cirrus, which represents less than 1/40 of the surface delimited by the circular INCAS track. For this reason we can realistically assume that the radiance came from an homogeneous source. Unfortunately, the aircraft's contrail intersected

125 FINESSE's field of view during the first measurement time slot, at 8:25 UTC, as shown in Fig. 4. By reconstructing the flight path, it appears that the aircraft, flying in circles, crossed its own contrail again, making it quite likely that the onboard sensors sampled part of the contrail itself. We will therefore take this into account in our analysis.
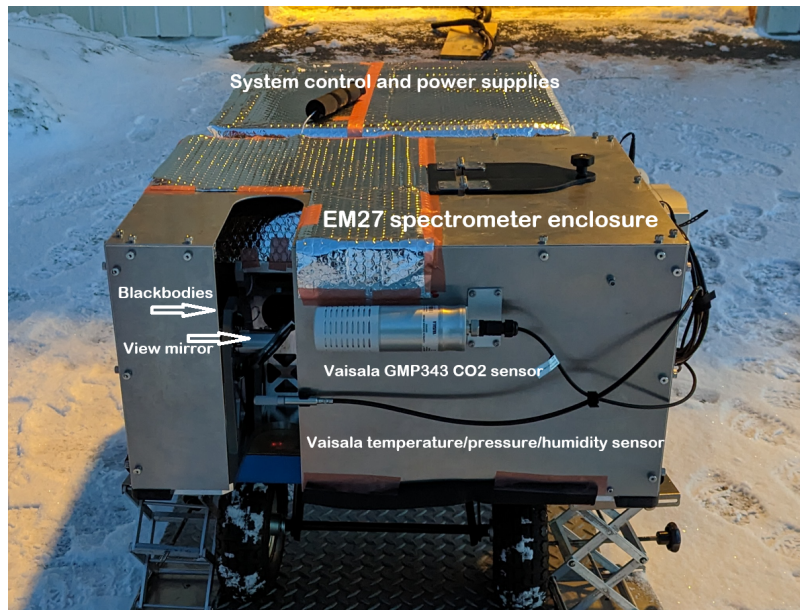
2.2 FINESSE spectrometer

The FINESSE spectrometer (see Fig. 5 deployed outside the ALOMAR facility) measured spectrally resolved radiances from

130 400-1500 cm^{-1} with a nominal spectral resolution of 0.5 cm^{-1}. The instrument consists of a commercial Bruker EM27 spectrometer coupled with a bespoke front-end pointing optics and calibration system. This enables the instrument to view in all directions from nadir through to zenith (Murray et al., 2024).
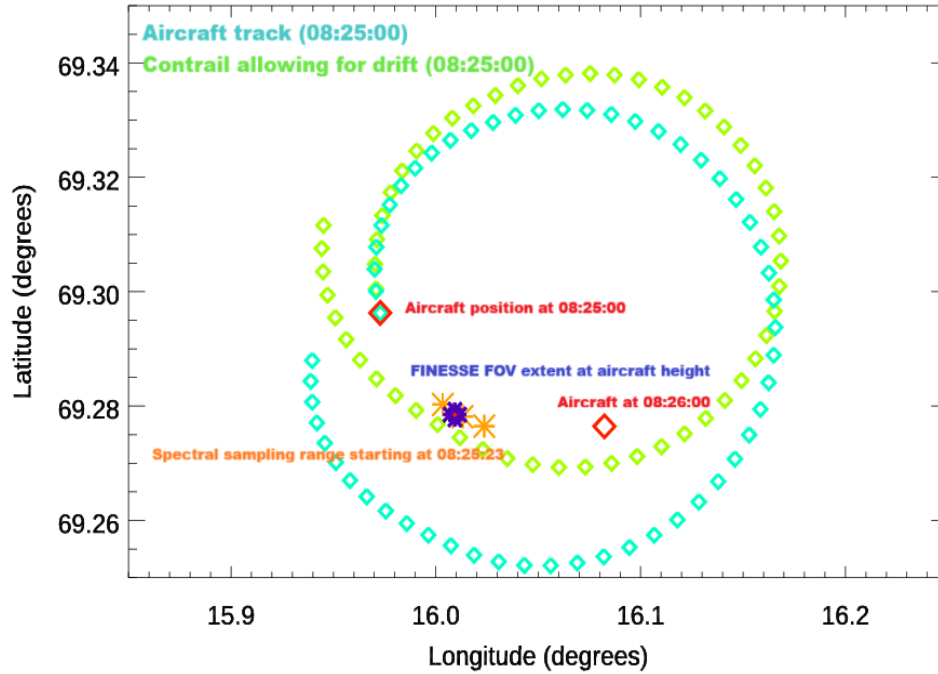
Figure 4. The turquoise diamonds map the aircraft track over the Alomar site up to 08:25:00 UTC, 30 seconds before the first overpass. We use photographs taken at this time and at 08:27:00 UTC, 30 seconds after the overpass to estimate the drift of the aircraft contrail, shown by the green diamonds. Extrapolating this to 08:26:30 indicates that at the time of the overpass the contrail formed earlier in the flight, to the South-West, is directly over Alomar at the time of the overpass, this time also coincides with a distinct rise in radiance at $900\,\mathrm{cm^{-1}}$, observed by FINESSE.

During the 17th February, the instrument was placed outside the ALOMAR building an hour prior to the aircraft overpass and operated in zenithal configuration, with measurements made between 07:30 and 12:00 UTC. The EM27 was configured
135 to acquire interferograms in groups of 40 scans. One scan, at $0.5\ \mathrm{cm^{-1}}$ resolution, takes 1.5 s to acquire. One fixed scene observation then takes 1 minute. The FINESSE control interface was initially set to acquire calibration scans of hot and ambient temperature blackbodies followed by 2 zenith views, this cycle of observations taking 4 minutes was repeated until just before the arrival of the aircraft at 08:15 UTC, when the number of zenith observations between calibrations was increased to 6.
140 Given the goal of the study the first step involved matching the FINESSE sky-views as closely as possible to the aircraft overflights. FINESSE has a beam diameter of 38 mm at its input window. This diverges with a full angle of 1.7; therefore, as noted earlier, the diameter of the FINESSE FOV at the cloud height was roughly 180 m. Given the INCAS aircraft speed of 85 $\mathrm{m\,s^{-1}}$ (Fig. 3) this implies that in the ideal case the aircraft would traverse the FINESSE FOV in around 2.1 seconds. In reality, there was always a slight mismatch between the location of the aircraft and the FINESSE FOV. For this analysis we consider
145 all FINESSE spectra (obtained through the Fourier transform of the interferograms) that were taken when the aircraft location

7

Figure 5. A front on view of FINESSE in its operational position outside the ALOMAR facility. The calibration blackbody targets, and scene selection mirror are seen within the spectrometer enclosure through the open system aperture. The EM27 input aperture is to the right of the mirror within the enclosure. Also highlighted are Vaisala sensors measuring the ambient atmospheric conditions. The system control and power supply unit is to the rear.

was within 1 km of the FINESSE FOV. Using this criterion, a subset of 11 spectra, temporally and spatially co-located with the other measurements, were selected between 8:25:23 UTC (30327 sec. since midnight, co-location 1) and 8:37:49 UTC (31069 sec. since midnight, co-location 11 (Table 1).

150 To help constrain the environmental conditions in the vicinity of FINESSE, two additional Vaisala probes are attached to the instrument casing. The Vaisala PTU303 probe measures pressure, temperature and relative humidity with quoted uncertainties of 0.1 mb, 0.3 C and 1%, respectively. The Vaisala GMP343 probe records the CO_2 mixing ratio. We make use of the average value recorded during the FINESSE observing period of 395 ppmv to scale the profile used in the radiative transfer simulations described in section 3.1. The temperature and humidity measurements are also used to help evaluate the FINESSE retrievals (section 4.2)

155 2.3 Ceilometer

The Met-Norway operated ceilometer (Lufft CHM15k) is permanently installed at the northerly tip of Andøya, approximately 6.3 km from ALOMAR and 4.4 km from Andøya Space (see Fig. 1). The ceilometer is designed to measure the backscattering profile of aerosols and clouds. The passage of cirrus clouds over ALOMAR is pictured in Fig. 6. The left panel of Fig. 7 shows the detection of broken cirrus over the site on the 17th February 2023. During the time of the selected FINESSE observations
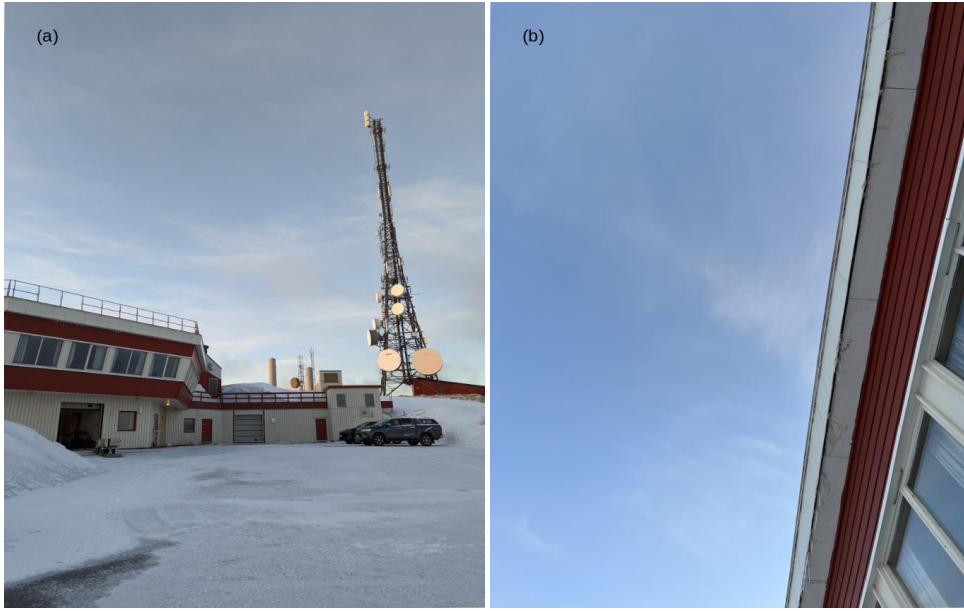
Figure 6. (a) View of ALOMAR with FINESSE visible right in front of the entrance of the facility (b) Passage of cirrus clouds over the site on 17th February 2023 at 07:45 UTC.

Table 1. Selected FINESSE spectra for the analysis

Co-location index	time UTC (hh:mm:ss)	sec. since midnight
1	08:25:23	30323
2	08:25:25	30325
3	08:25:27	30327
4	08:25:29	30329
5	08:25:31	30331
6	08:25:33	30333
7	08:37:41	31061
8	08:37:43	31063
9	08:37:45	31065
10	08:37:47	31067
11	08:37:49	31069

160 (denoted by the black vertical dashed lines), above the boundary layer the strongest ceilometer returns emanate from between 6-7 km, peaking, in agreement with the aircraft observations, at around 6.7 km (Fig. 7, right panel). Even though the peak of the signal is located a about 6.7 km, non-negligible signal is present at the lower layers, down to about 6 km of altitude. This was also confirmed by the detection of ice crystals at 6 km by the probes on board the aircraft. These backscattering profiles

are used to fix the cirrus top and bottom heights (CTH and CBH) used in the radiative transfer simulations described in detail in section 3.1.
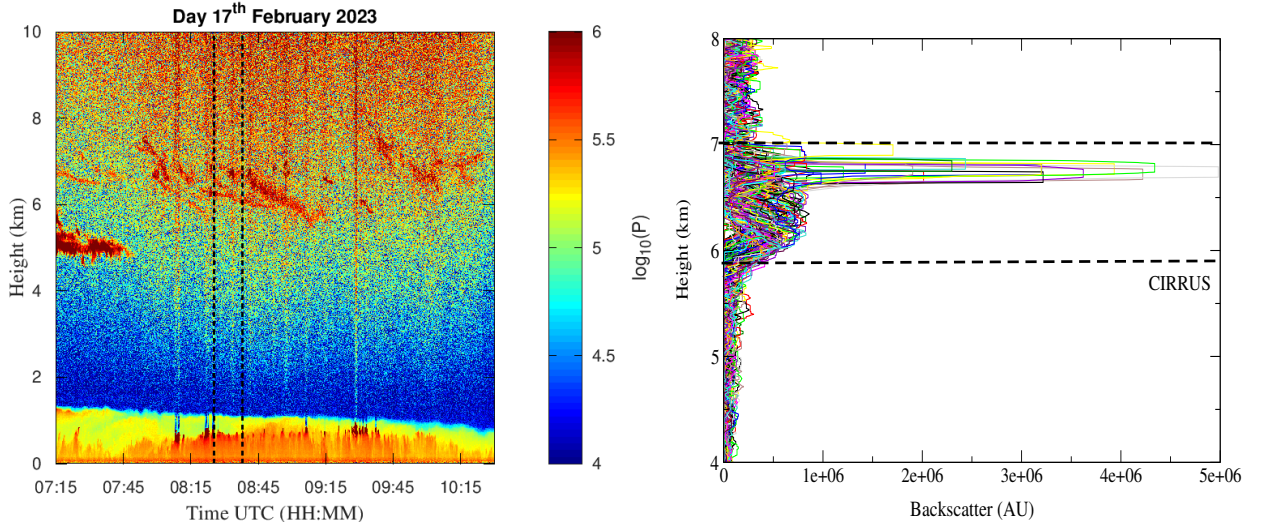
Figure 7. Left: Logarithmic backscattering signal (P, in arbitrary unit (AU)) detected by the Met-Norway ceilometer on 17th February 2023 showing the passage of cirrus clouds between 7:15 and 10:30 UTC. The dashed vertical black dashed lines at 8.25 and 8.38 UTC delimit the time window of the FINESSE measurements selected for analysis. Right: Individual backscattering profiles obtained during the 8.25-8.38 UTC time window.

2.4 HATPRO radiometer

The Humidity And Temperature PROfiler version G4 (HATPRO; RPG Radiometric Physics GMBH, DE) is a microwave radiometer designed as a network suitable low-cost passive instrument able to observe liquid water path (LWP), column water vapour and humidity and temperature profiles with high temporal resolution of up to 1 s. The HATPRO is equipped with two bands, K and V, one (K) in the range 22–31 GHz, and one (V) covering frequencies between 51-58 GHz (Löhnert et al., 2009). Both the K and V bands are composed of seven channels. K provides humidity, column water vapour and LWP information by exploiting pressure broadening of the 22.235 GHz H_2O line. The V band is used to generate temperature information. Comparisons of HATPRO retrievals made as part of the Multidisciplinary drifting Observatory for the Study of the Arctic Climate expedition with radiosonde launches show agreement in integrated water vapour to within 0.35 kg m^{-2} when values are lower than 5 kg m^{-2}, conditions similar to those experienced during MC2-ICEPACKS. The same analysis suggests a marked overestimate of humidity at the surface, switching to a small underestimate by 2-3 km. For temperature, biases were of the order 0.7-1.8 K for the lowest 2 km of the atmosphere (Walbröl et al., 2022).

3 Methodology and retrieval techniques

Our intent is to assess the consistency of products retrieved from the FINESSE radiances with equivalent information derived
from the available in-situ airborne and ancillary ground-based observations. To this end, three retrieval techniques have been
applied to the available datasets: the first to the FINESSE spectral radiances to retrieve the cirrus effective diameter (D_{ei})
and visible optical depth (OD), together with the atmospheric profiles of water vapour and temperature and the ozone total
column (Section 3.1); the second to the ceilometer backscattering signal to retrieve the cirrus extinction profiles and then the
OD (Section 3.2); the third to the HATPRO radiometer measurements to retrieve the vertical profiles of water vapour and
temperature (Section 3.3).

3.1 Retrieval of atmospheric and cloud parameters from FINESSE spectral radiances

The FINESSE analysis was performed using the Simultaneous Atmospheric and Clouds Retrieval (SACR) code (Di Natale
et al., 2020). To adapt the code to simulate the FINESSE radiances we integrated the instrument line shape described in
Murray et al. (2024) within the SACR Forward Model (FM) so that the high-resolution spectral radiances generated by the
FM were correctly convolved to mimic the spectrum measured by FINESSE. Unless otherwise stated the retrievals exploit the
spectral range 400-1500 cm^{-1}.

The FM simulations were performed on a vertical grid fixed between 0.37 (ground level) and 70 km, to account for the
radiative contribution of stratospheric ozone. To resolve detail within the boundary layer, a finer vertical resolution of 0.02 km
was chosen close to the surface, reducing to 1 km at the highest altitudes. The cirrus cloud was modeled by fixing the position
between 6-7 km and considering multiple layers with an internal vertical resolution of 0.1 km. The initial guess and a-priori for
temperature and water vapour profiles and ozone total column used in the retrieval, were built by perturbing the corresponding
profiles provided by ECMWF ReAnalysis-5 (ERA5) (Hersbach et al., 2020) database. Water vapour was perturbed by assuming
the vertical distribution of uncertainties used for The Michelson Interferometer for Passive Atmospheric Sounding (MIPAS)
analysis (Remedios et al., 2007)); temperature and ozone were perturbed, respectively, by 1% and 10% of the corresponding
profiles. The concentrations of other minor gases were provided by the Initial Guess-2 (IG2) dataset (Remedios et al., 2007),
with CO_2 scaled to the value provided by the FINESSE Vaisala probe. A-priori estimates for D_{ei} and OD were set equal to
80 μm and 0.5, respectively (values that are slightly higher than those expected for thin cirrus clouds) assuming uncorrelated
errors as large as 100%. These values were also set as initial guesses in the analysis.

Table 2 summarises the parameters retrieved using FINESSE radiances, the initial guess and a priori values used in the
retrieval procedure, the a priori errors considered, the alternative source/measurements providing the parameters with which
we validated our results or we used to fix values in the radiative transfer simulations.

3.1.1 Simulation of cirrus cloud spectral radiance

The SACR FM combines spectral gaseous ODs generated by the Line-By-Line Radiative Transfer Model (LBLRTM v12.15)
(Clough et al., 2005) with a specific code based on the two stream δ-Eddington approximation which can account for multiple

Table 2. Parameters retrieved from FINESSE spectra, the initial guess/a-priori, sources used to validate the retrieval products, and the unretrieved parameters used in the radiative transfer simulations.

FINESSE retrieved parameter	initial guess/a priori	a priori error	alternative source	not retrieved parameter
D_{ei}	80 μm	100%	INCAS KA	habit type, T_{cld}
OD	0.5	100 %	CEILOMETER	CTH, CBH
T profile	ERA5 perturbed of 1%	1.5%	ERA5	-
T @ ground	ERA5 perturbed of 1%	1.5%	VAISALA	-
WV profile	ERA5 perturbed following MIPAS analysis	100%	ERA5	-
WV @ ground	ERA5 perturbed following MIPAS analysis	100%	VAISALA	-
O_3 total column	ERA5 perturbed of 10%	100%	ERA5	-
-	-	-	IG2 + VAISALA	CO_2 profile
-	-	-	IG2	N_2O, CH_4, CO profiles

scattering from particles. SACR is designed such that it can ingest the single scattering properties of spherical water droplets alongside those of ice crystals with different habits. Ice crystal properties are taken from the Yang et al. (2015) databases that tabulate the extinction/absorption efficiencies ($Q_{a,ei\nu}$), the single scattering albedos (ω_ν) and the asymmetry factors (g_ν) together with the volumes (V_h) and projected areas (A_h) of nine crystal habits (the subscript h denotes the habit), namely solid/hollow bullet rosettes (SBR/HBR), solid/hollow columns (SCL/HCL), plates (PL), droxtals (DX), spheroids (SPH), aggregates (AGG) (10-plates and 8-columns), as a function of the crystal maximum length (L) in the range 2–10000 μm and wavenumber (ν) in the range 100–5000 cm^{-1}. To model the cirrus SACR uses the averages of the single scattering properties integrated over assumed particle size (n(L)) and habit (f_h(L)) distributions tabulated in the form of look-up tables (LUTs) as a function of D_{ei}. D_{ei} is defined as follows (Yang et al., 2005):

$$D_{ei} = \frac{3}{2} \frac{\sum_{h=1}^{N} \int_{L_{\min}}^{L_{\max}} f_h(L) V_h(L) n(L) dL}{\sum_{h=1}^{N} \int_{L_{\min}}^{L_{\max}} f_h(L) A_h(L) n(L) dL} \tag{1}$$

f_h is defined such that $\sum_{h=1}^{N} f_h = 1$ at each particle length L and N is the total number of habits. The averages of the single scattering properties $\langle Q_{a,ei} \rangle_\nu$, $\langle g_i \rangle_\nu$ and $\langle \omega_i \rangle_\nu$ are given by:

$$\langle Q_{a,ei} \rangle_\nu = \frac{\sum_{h=1}^{N} \int_{L_{min}}^{L_{max}} f_h(L) Q_{a,ei,\nu}(L)(L) A(L) n(L) dL}{\sum_{h=1}^{N} \int_{L_{min}}^{L_{max}} f_h(L) A(L) n(L) dL} \tag{2}$$

$$\langle g_i \rangle_\nu = \frac{\sum_{h=1}^{N} \int_{L_{min}}^{L_{max}} f_h(L) g_i(L) Q_{si,\nu}(L) A(L) n(L) dL}{\sum_{h=1}^{N} \int_{L_{min}}^{L_{max}} Q_{si,\nu}(L) f_h(L) A(L) n(L) dL} \tag{3}$$

$$\langle\omega_i\rangle_\nu = 1 - \frac{\langle Q_{ai}\rangle_\nu}{\langle Q_{ei}\rangle_\nu} \tag{4}$$

where $Q_{si,\nu} = Q_{ei,\nu} - Q_{ai,\nu}$ is the scattering efficiency and $L_{min} = 2\ \mu$m and $L_{max} = 10000\ \mu$m represent the limits of maximum lengths. Finally, the expression of the OD for a generic wavenumber (OD_ν) is given by:

$$OD_\nu = \frac{3 \cdot IWP}{D_{ei}\rho_i}\frac{\langle Q_{ei}\rangle_\nu}{2} = OD\frac{\langle Q_{ei}\rangle_\nu}{2} \tag{5}$$

with IWP the integrated water path and ρ_i = 917 kg m^{-3} the ice density.

3.1.2 Building the look-up tables of single-scattering average properties

To build the LUTs of the cirrus clouds average properties as a function of the effective diameter and wavenumber we applied Eqs. (1)–(4) and assumed a-priori a monomodal Γ-like PSD (Platnick et al., 2017; Turner, 2005) that varies analytically with the modal parameter L_m:

$$n(L) = N_o L^\mu e^{-(3+\mu)\frac{L}{L_m}} \tag{6}$$

where the quantity $L_m/(3+\mu)$ represents the mode of the distribution. In this way, we obtained a set of Γ PSDs (each corresponding to a D_{ei}) to use in Eqs. (1)–(4) simply by defining a vector of continuous values of L_m between 2 and 10000 μm . The intercept parameter N_o does not need to be evaluated since it appears in both the numerator and denominator in Eqs. (1)–(4) while the dispersion coefficient μ, that is temperature dependent, must be set. This coefficient was assessed by fitting the average of the INCAS KA measured PSDs (see section 2.1) with the function described by Eq. 8; we found a best fit value of $\mu = 2$ and we used it in Eqs. (1)–(4) to create the LUTs for four habit distributions described below.

Fig. 8 shows that the ice crystals sampled on the 17th February flight were predominantly of bullet rosette morphology. However, there are also a minority of crystals, below $\sim$50 μm of maximum length, which are difficult to define from the photographs. For these crystals the aspect ratio tends to be close to 1. For the second sequence of aircraft measurements we make the assumption that these crystals are 100% plate-like, consistent with previous work performed over the Antarctic Plateau (Del Guasta, 2022). For the first sequence of measurements at 8:25 UTC when the FINESSE FOV intersected the INCAS contrail, we assume they are 50% plate-like and 50% droxtal-like. This assumption stems from the fact that aircraft contrails are formed by water vapor or combustion particulates emitted by the engines, which either sublimate instantaneously in the former case or act as condensation nuclei in the latter. With these assumptions we define the measured habit distribution at 8:25 and 8:37 UTC as follows:

$$f_h(L) = \begin{cases} BR & L > 50\,\mu\text{m} \\ \frac{1}{2}DX + \frac{1}{2}PL & @\,8:25\,UTC, \quad PL \quad @\,8:37\,UTC \quad L \leq 50\,\mu\text{m} \end{cases} \tag{7}$$

13
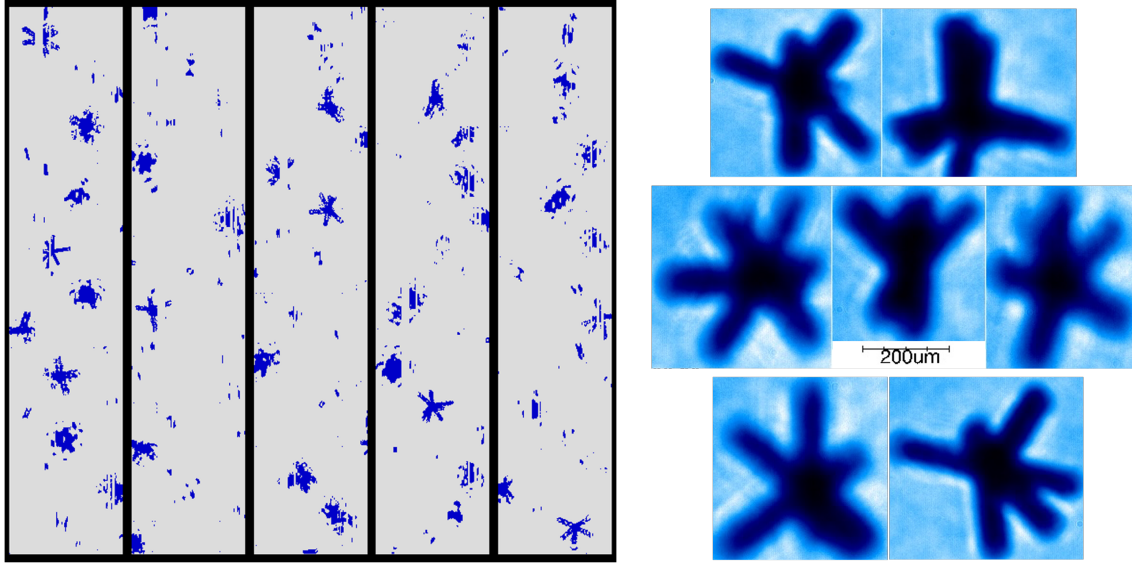
Figure 8. Examples of the ice crystals observed inside the cirrus layer by the INCAS KA on 17th February 2023 at 8:20 UTC. Images from the 10 μm-resolution channel of the 2D-S (left) where the width of each strip is 1280 μm and the CPI (right) are shown

where BR denotes generic bullet rosettes. The habit distribution in Eq. (7) is used in Eqs. (1)–(4) together with the PSDs to build the LUTs of the cirrus cloud average properties as a function of the effective diameter and wavenumber. To test the impact on the retrieval results of mixing other habits we also considered four habit distributions: two by assuming single HBR and SBR, denoted as f1h and f2h, and the others, f_{3h} and f_{4h}, by mixing them homogeneously and also adding solid columns. Considering Eq. (7), these habit distributions can be summarized as follows:

$$f_h(L) = \begin{cases} \text{HBR} & L > 50\,\mu\text{m} \\ \frac{1}{2}\text{DX} + \frac{1}{2}\text{PL} \quad @8{:}25\,\text{UTC}, \quad \text{PL} \quad @8{:}37\,\text{UTC} & L \le 50\,\mu\text{m} \end{cases} \tag{8}$$

$$f_h(L) = \begin{cases} \text{SBR} & L > 50\,\mu\text{m} \\ \frac{1}{2}\text{DX} + \frac{1}{2}\text{PL} \quad @8{:}25\,\text{UTC}, \quad \text{PL} \quad @8{:}37\,\text{UTC} & L \le 50\,\mu\text{m} \end{cases} \tag{9}$$

$$f_h(L) = \begin{cases} \text{HBR} + \frac{1}{2}\text{SBR} & L > 50\,\mu\text{m} \\ \frac{1}{2}\text{DX} + \frac{1}{2}\text{PL} \quad @8{:}25\,\text{UTC}, \quad \text{PL} \quad @8{:}37\,\text{UTC} & L \le 50\,\mu\text{m} \end{cases} \tag{10}$$

$$f_h(L) = \begin{cases} \text{HBR} + \frac{1}{3}\text{SBR} + \frac{1}{3}\text{SCL} & L > 50\,\mu\text{m} \\ \frac{1}{2}\text{DX} + \frac{1}{2}\text{PL} \quad @8{:}25\,\text{UTC}, \quad \text{PL} \quad @8{:}37\,\text{UTC} & L \le 50\,\mu\text{m} \end{cases} \tag{11}$$

3.1.3 Retrieval algorithm

The SACR retrieval algorithm is based on the optimal estimation (OE) approach and the Levenberg-Marquardt iterative formula Marquardt (1963); Rodgers (2000). Initially we use FINESSE observations over the spectral range 400–1500 cm^{-1} to perform the retrieval. The atmospheric state vector in the presence of cirrus clouds used by SACR is:

$$\mathbf{x} = (\mathrm{D_{ei}}, \mathrm{OD}, \mathbf{U}, \mathbf{T}, O_3, \beta) \tag{12}$$

where $\mathbf{U}$ and $\mathbf{T}$ denote the vectors of the selected retrieval levels for the water vapour and temperature profiles, O_3 indicates the ozone total column, and β a frequency stretch (usually of the order of 10^{-6}) which takes into account the shift due to the finite internal aperture (Ω) given by $\nu(1 - \frac{\Omega}{4\pi})$ (Davis et al., 2001), and the effect due to possible instability of the reference laser (Palchetti et al., 2016).
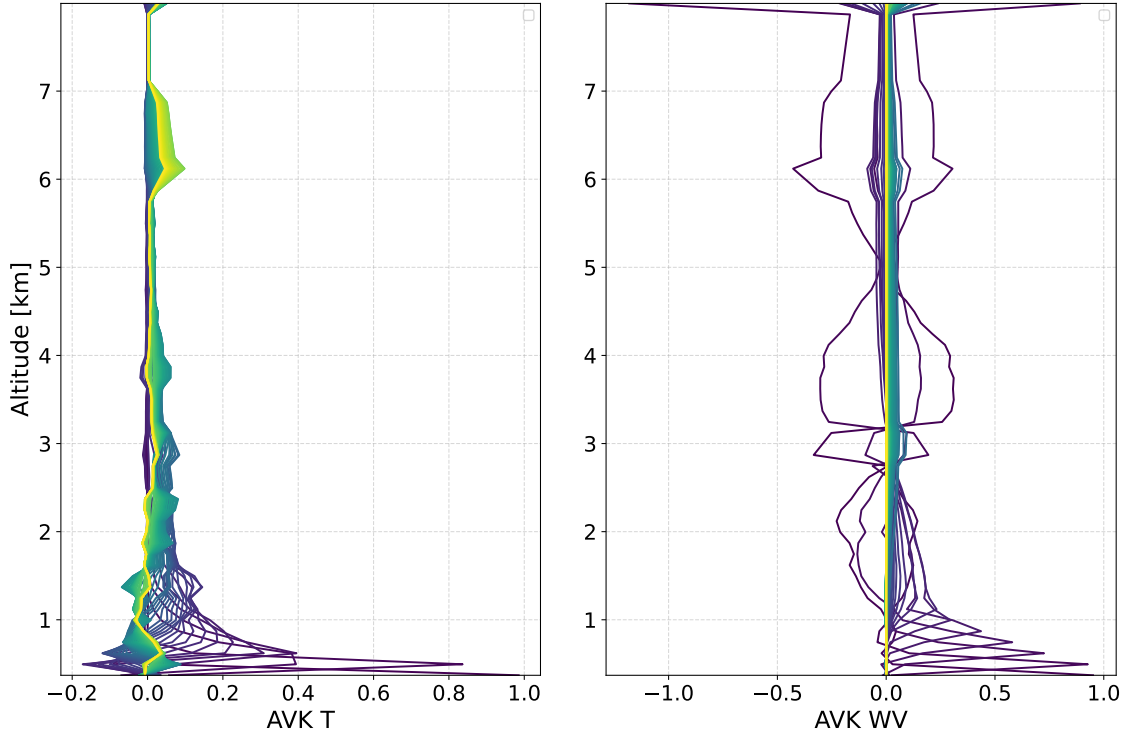
Figure 9. Left panel: vertical distribution of averaging kernels of temperature. Right panel: same for water vapour.

The levels in $\mathbf{U}$ and $\mathbf{T}$ were set to 0.37 (ground level), 0.60, 0.80, 1.00, 1.40, 1.80, 2.0, 3.0, 4.0 km for water vapour and 0.37, 0.39 and 0.80 km for temperature, respectively. These levels were selected by studying the sensitivity to temperature and water vapour from the vertical distribution of the averaging kernels (AK) as shown in Fig. 9. Sensitivity is predominantly limited to below 1 km and 4 km for temperature and water vapour, respectively. The study provides 3 and 7 total DOFs for

temperature and water vapour on average. In each case, above the highest level the profile is rescaled keeping the shape of the original profile. The levels were chosen so as to retrieve profile structure without over-constraining the solution with a-priori information, avoiding non-physical fluctuations.

The algorithm finds the solution as that which minimises the cost function:

$$\chi^2 = (\mathbf{y} - \mathbf{F}(\mathbf{x}))^T \mathbf{S}_y^{-1} (\mathbf{y} - \mathbf{F}(\mathbf{x})) + (\mathbf{x} - \mathbf{x}_a)^T \mathbf{S}_a^{-1} (\mathbf{x} - \mathbf{x}_a) \tag{13}$$

where $\mathbf{y}$, $\mathbf{F}$ and $\mathbf{x}_a$ denote the vector of the FINESSE measurements, the forward model and the a-priori information, respectively. The a-priori correlation lengths for water vapour and temperature profiles were set to 0 and 2 km, respectively, to avoid over-constraining the retrieval and because the temperature shows a smooth linear behavior with altitude. However, the correlation between the two first temperature levels was set to 0 because the very first layers can be locally affected by the presence of nearby thermal sources.

The cost function is minimized with the LM iterative formula as follows (Rodgers, 2000):

$$\mathbf{x}_{i+1} = \mathbf{x}_i + [\mathbf{K}_i^T \mathbf{S}_y^{-1} \mathbf{K}_i + \gamma_i \mathbf{D}_i + \mathbf{S}_a^{-1}]^{-1} [\mathbf{K}_i^T \mathbf{S}_y^{-1} (\mathbf{y} - \mathbf{F}(\mathbf{x}_i)) - \mathbf{S}_a^{-1} (\mathbf{x}_i - \mathbf{x}_a)] \tag{14}$$

where $\mathbf{S}_y$ and $\mathbf{S}_a$ are the Variance Covariance Matrices (VCMs) of the measurements containing the quadratic sum of the NESR and the calibration error, and the a-priori information; γ_i is the damping factor at the i-h iteration, $\mathbf{K}_i$ represents the Jacobian matrix of $\mathbf{F}$ and $\mathbf{D}_i$ is a diagonal matrix as described in Di Natale et al. (2020). The FINESSE measurement noise is considered uncorrelated and given by the noise equivalent spectral ratio (NESR) calculated as discussed in Murray et al. (2024). Convergence is reached when the variations in χ^2 are less than 1‰. The retrieval errors of the parameters are contained in the VCM given by the relation (Rodgers, 2000):

$$\mathbf{S}_x = (\mathbf{K}^T \mathbf{S}_y^{-1} \mathbf{K} + \mathbf{S}_a^{-1})^{-1} \tag{15}$$

where $\mathbf{K}$ is the Jacobian matrix at the last iteration.

3.1.4 Accounting for calibration uncertainty

We chose to study a-posteriori the effect of the systematic error due to FINESSE calibration uncertainty, since including the spectral correlation effect in the VCM of measurements could lead, based on experience, to the retrieval algorithm becoming stuck in a local minimum and so to incorrect results. Our initial retrievals from FINESSE assume no calibration uncertainty on the observed radiances. We then repeat the retrievals systematically increasing and reducing the radiances with their calibration uncertainties (Fig. 10). The average between the maximum and the minimum differences of the retrieval products with respect to those obtained from the original retrieval is assumed to be the contribution of the calibration error. Total retrieval errors are then calculated as the square root of the quadratic sum of the retrieval error (equation 15) and the calibration error. These are the values reported in Section 4.
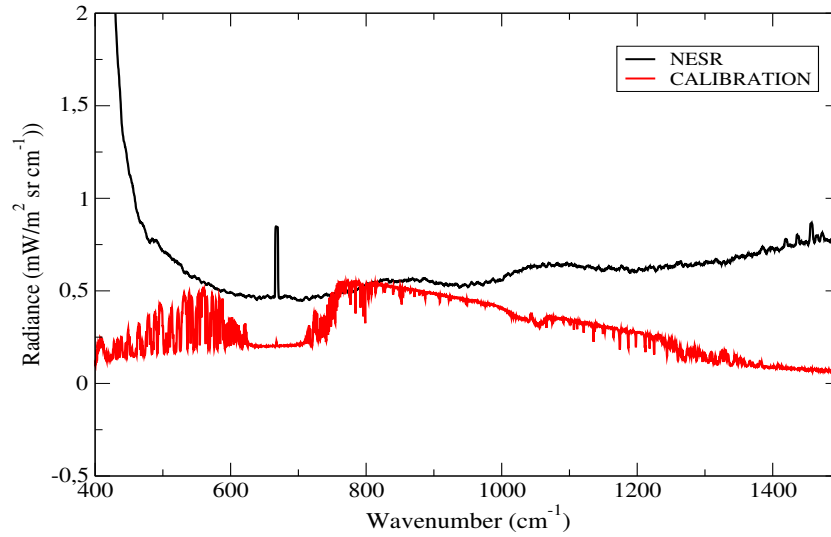
Figure 10. Comparison of the FINESSE Noise Equivalent Spectral Ratio (NESR, black curve) and the calibration systematic error (red curve).

3.2 Klett method for retrieving cirrus clouds optical depth from ceilometer backscattering signal

The cirrus OD can also be retrieved from the ceilometer backscattering signal, that we call P, as a function of the height z by using the Klett inversion method (Klett, 1981, 1985). Since this problem involves only one equation and two unknowns, namely the backscatter (β_e) and the extinction (σ_e), the relationship that binds them must be assumed. A common solution is
305 to assume a power-law relationship with a generic exponent k, called the backscatter-extinction coefficient ratio, as follows:

$$\beta_e(z) = C \cdot \sigma_e(z)^k \tag{16}$$

where C is a constant and k depends on the laser frequency, the aerosol composition and the inhomogeneity of the layers, particularly the variability of the aerosol PSD, the particles shape and the mixing with the air, and is affected by multiple-scattering effect (Del Guasta et al., 1993; Elouragini, 1995). k generally ranges between 0.67–1.00 (Klett, 1981; Elouragini,
310 1995), due to the complexity of particle shapes and their inhomogeneous dimensions and distributions: preliminary tests by varying k suggested a value of k=1 was most appropriate for our analysis here. Using the relationship of Eq. (16), Klett's lidar solution for the cloud extinction profile ($\sigma_c(z)$) is obtained as a function of the height z as follows (Klett, 1981):

$$\sigma_c(z) = \frac{\exp[\frac{S(z)-S_r}{k}]}{\sigma_r^{-1} + \frac{2}{k}\int\limits_z^{z_r}\exp[\frac{S(z')-S_r}{k}]dz'} - \sigma_m(z) \tag{17}$$

17

where $S(z) = \ln(P(z)z^2)$ represents the logarithmic range-corrected signal (LRCS), $\sigma_m(z)$ is the molecular extinction due to the gas contribution derived from the atmospheric profiles, S_r and σ_r denote the LRCS and the extinction at a reference height z_r that must be fixed above the CTH, where the backscattering is completely molecular in origin. Because of the noisiness of the signal above the CTH and the sensitivity of the solution to σ_r, a signal smoothing process, such as a moving average, is necessary to make the solution more stable. From the extinction profile the optical depth is obtained as the integral over the cloud geometrical thickness:

$$\text{OD} = \int\limits_{\text{CBH}}^{\text{CTH}} \sigma_c(z)dz \tag{18}$$

Since the solution is sensitive to σ_r we repeated the retrieval procedure, varying the choice of z_r above the CTH. We used 10 heights from 0.1 km to 1 km in steps of 0.1 km and report the average value as the ceilometer derived OD. This approach also allows the evaluation of the retrieval error for each scenario as the standard deviation of the retrieved OD divided by $\sqrt{10}$, the number of heights chosen.

3.3 Retrieval of temperature and water vapour vertical profiles from HATPRO measurements

The HATPRO temperature and humidity profiles are based on statistical retrievals (**?**). Using a twenty year ERA5 dataset for Andenes, a quadratic regression model was trained relating atmospheric profiles and simulated brightness temperatures. The "pyMakeRetrieval" software package was used to create temperature and humidity retrievals (Foth, 2024).

3.4 Calculation of the effective diameters of ice crystals inside cirrus clouds from INCAS measurements

The INCAS KA measurements offer a check of the retrieval of D_{ei} from the FINESSE spectral radiances by directly substituting the observed PSDs measured during the flight into Eq. (1). As noted in section 3.1.1, the calculation depends on the specific habit distribution assumed. We repeat calculations for the four habit distributions described in Eqs. (1)–(4) for observations taken by the INCAS KA between 08:19 and 09:00 UTC, neglecting periods at the highest 'cloud' altitudes, in the 20 m above 6.77 km where tenuous and highly variable signals were reported. The slightly longer time-span in comparison to the selected FINESSE measurements is to enable sufficient statistics to be generated. Fig. 11 shows the effective diameters calculated using INCAS KA PSDs as a function of the height inside the cirrus cloud.

To assess the accuracy of the PSDs measured by the INCAS KA, and estimate the systematic error that affects the effective diameter due to the bin sampling of the PSD, we took into account that the measured PSD associates the same number of ice particles within a specific crystal length bin equal to 50 μm , starting from a minimum length of 25 μm . We considered three PSDs normalized to the respective maxima and corresponding to three different effective diameters, the smallest one equal to 25 μm , the middle one equal to 49 μm and the largest one equal to 73 μm . Since we want to assess how much the bin sampling limits the accuracy, we need to find the analytic functions that reproduce the data distribution as closely as possible. We fitted the first PSD with the mono-modal Γ-function in Eq. (6) while the second and third were fitted with a bi-modal Γ-function:
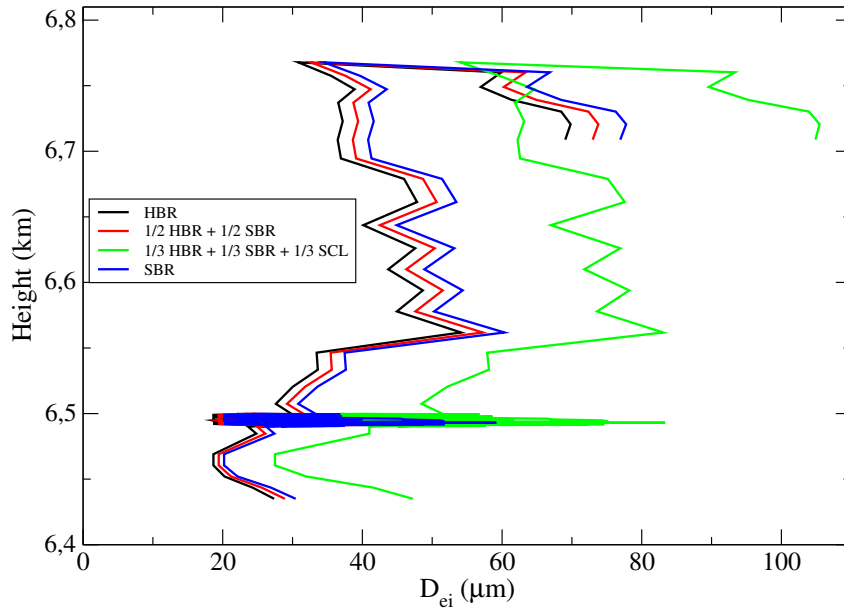
Figure 11. Vertical distribution of the derived ice crystal effective diameters calculated from the INCAS KA observed ice crystal PSDs and using the Yang et al. (2013) single scattering properties databases and the habit distribution given by Eqs. (1)–(4).

$$n(L) = N_1 L^{\mu_1} e^{-(3+\mu_1)\frac{L}{L_{m1}}} + N_2 L^{\mu_2} e^{-(3+\mu_2)\frac{L}{L_{m2}}} \tag{19}$$

345   obtaining the best fit curves shown in Fig. 12. For each PSD we calculated the difference in the value of the effective diameters obtained by using the measured PSD and the corresponding fitted curve; then we selected the maximum difference for the 3 cases, which was approximately 5 μm . This corresponds to the systematic error induced by the bin approximation implicit in the INCAS KA data. Finally, we added the statistical standard deviation on the average effective diameters obtained from the selected INCAS PSDs, equal to 1 μm . The two errors, systematic and statistical, were summed in quadrature to give

350   a combined uncertainty of $\sim$5 μm on the effective diameters derived from the INCAS measurements.

4   Results

4.1   Water vapour and temperature profiles

Fig. 13 shows a comparison of the retrieved profiles of temperature and water vapour from the FINESSE observations at 08:25 UTC with co-located ERA5 profiles (Hersbach et al., 2020). For a fairer comparison, the ERA5 data are convolved with the

355   appropriate averaging kernels. In general, relative to the first guess, the information from FINESSE tends to moisten the lowest 1 km of the atmosphere and dry the layer between 2-3 km. This behavior is consistently seen for all 11 cases identified in Table
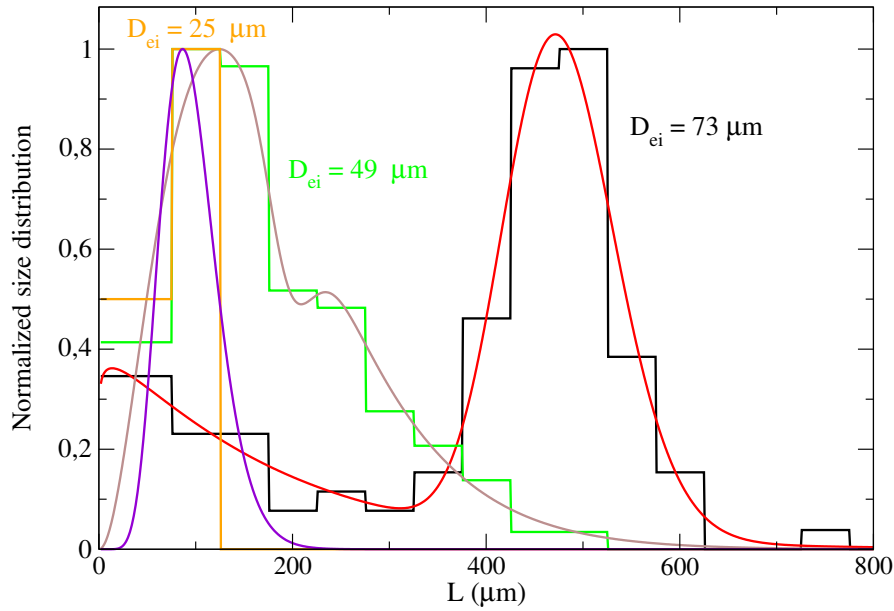
Figure 12. Three examples of PSDs normalized to the respective maxima measured by the INCAS KA (black, green and orange histograms) with the D_{ei} calculated assuming the habit distribution in Eq. (7) and the fitting functions (red, brown and violet curves)

1. Although we do not possess a 'true' water vapour profile, we can see that the uncertainties on the retrieval typically overlap the ERA5 estimates. For temperature, the retrievals at the lowest levels are shifted warmer and closer to the ERA5 values. The in-cloud temperature structure recorded by the INCAS KA temperature probe also shows excellent overlap with ERA5, giving additional confidence in the latter as a realistic representation of the atmospheric state. Moreover, even though the upper part of the retrieved temperature profile is only rescaled with respect to the highest retrieval level, keeping the shape of the initial guess profile, as described in section 3.1.3, the matching with the INCAS KA data provides a very good indication that the retrieval is consistent and the atmospheric state fairly characterised and represented in the simulations. The average difference between the retrieved and INCAS KA temperature profile is 0.37 K and all differences vary inside the interval -1 to 1 K.

For completeness Fig. 13 also includes the HATPRO retrieved profiles. The temperature retrievals tend to show a cold bias relative to ERA5 between 1-3 km, switching to a more pronounced warm bias above 5 km. As might be expected in light of previous studies, the water vapour profile is too smooth, and not able to capture the vertical structure, particularly the dry layer between 1-3 km.

4.2 Near-surface temperature and water vapour mixing ratios; total precipitable water and total column ozone

Fig. 14 provides a comparison between water vapour concentrations and temperature measured by the FINESSE Vaisala probes, the precipitable water vapour from the HATPRO and corresponding information derived from the FINESSE spectra and ERA5 data. A comparison of the ERA5 total column ozone with the equivalent FINESSE retrievals is also provided.
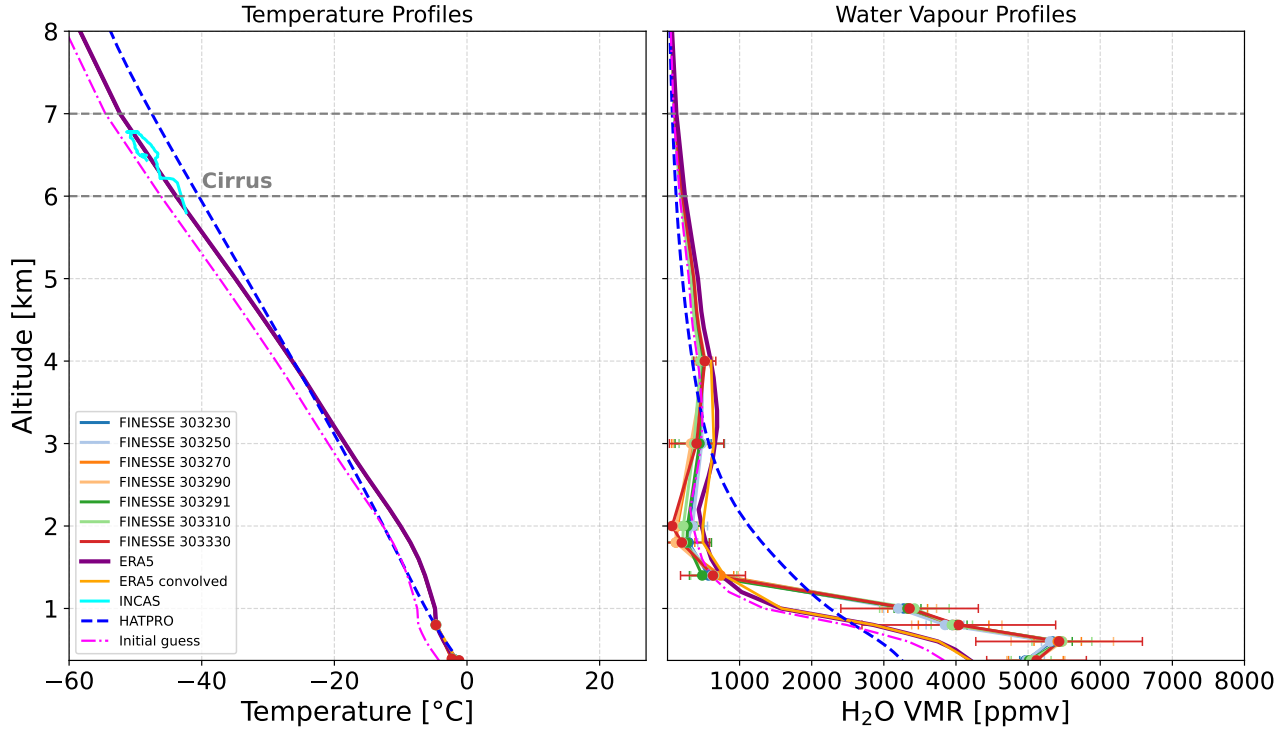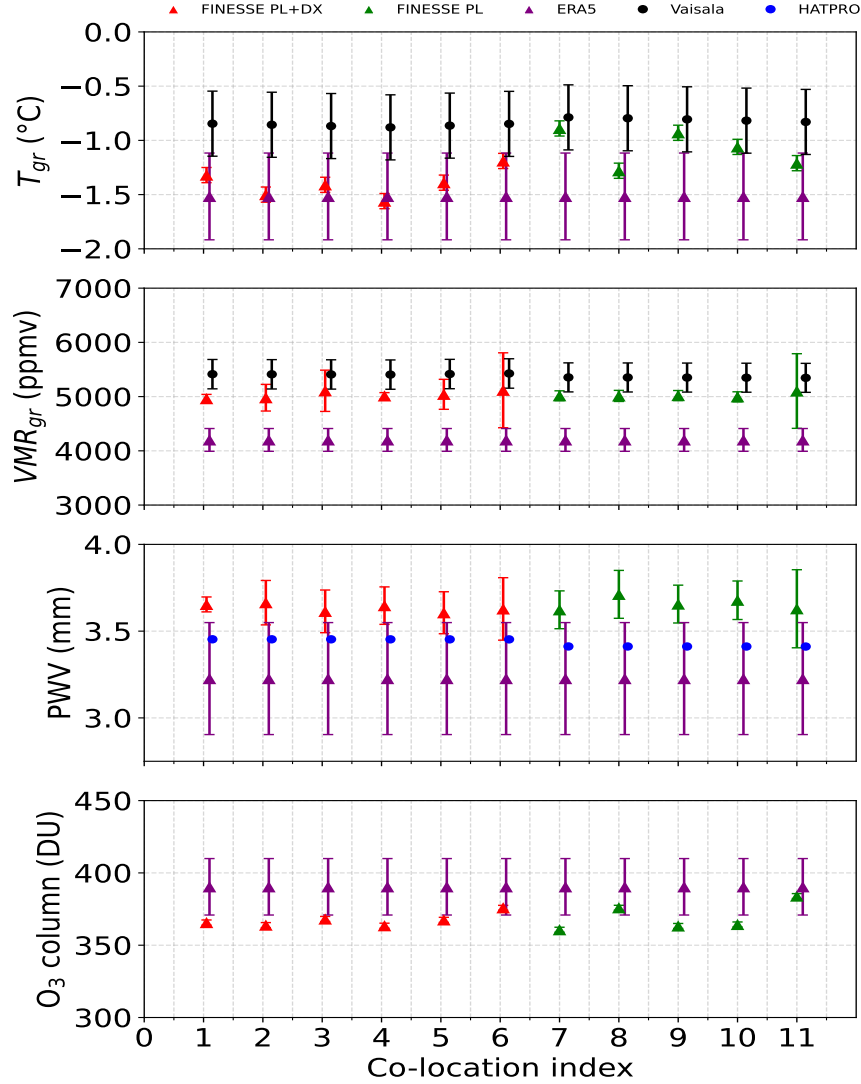
Figure 13. Left panel: comparison of the retrieved temperature profiles from FINESSE spectrum (solid lines) for the sequence at 08:25 UTC of 17 February 2023 with those provided by ERA5 (violet solid line), ERA5 convolved with the averaging kernels at the last iteration (orange solid line), INCAS KA (cyan solid line), and HATPRO radiometer (dashed blue line); in magenta the initial guess/a-priori is also reported. Right panel: same as the left panel but for water vapour profiles. The cirrus location is denoted by the dashed horizontal lines.

Considering near-surface temperature, FINESSE retrievals tend to sit between the values recorded by the Vaisala sensor and that given by ERA5 (Fig. 14, top panel). For the first five scenarios, when the overhead cirrus was optically thicker (Fig. 15), the FINESSE retrievals tend to show better agreement with the ERA5 value. Meanwhile, with thinner cirrus overhead they typically show an improved agreement with the Vaisala data (scenario 7-11). In all cases the difference between the FINESSE products and Vaisala data is lower than 0.7 K. The near-surface water vapour volume mixing ratios (VMR) obtained from the FINESSE retrievals show good agreement with the Vaisala probe data (Fig. 14, second panel). In contrast, ERA5 appears to underestimate the VMR for all scenarios, with differences reaching up to 1000 ppmv. The corresponding uncertainties for ERA5 quantities are assessed in Hersbach et al. (2020); Dragani et al. (2017); Bell et al. (2021).

The tendency for ERA5 to underestimate near surface water vapour relative to FINESSE is also reflected in comparisons of precipitable water vapour (PWV) (Fig. 14, third row), with a low bias which is on the order of 10% in this relatively dry environment. HATPRO PWV retrievals show values which sit between the FINESSE and ERA5 estimates but are typically

Figure 14. Top panel: comparison of the temperature at ground retrieved from FINESSE spectra (red and green triangles), measured by the Vaisala probe (black dots) and ERA5 (violet triangles) for each scenario. Second panel: same comparison as the temperature but for water vapour mixing ratio (VMR). Third panel: comparison of precipitable water vapour (PWV), retrieved from FINESSE (red and green triangles), from integrated HATPRO retrievals (blue dots) and from ERA5 (violet triangles). Bottom panel: comparison of the ozone total column retrieved from FINESSE and provided by ERA5.

closer to the former. Finally, the lowest panel of Fig. 14 indicates that the total column ozone retrieved from FINESSE is close
385   to the values obtained from ERA5 ozone profiles even though a bias of about 20 DU is present.

4.3   Cloud parameters

4.3.1   Optical Depths

The cirrus OD was retrieved independently from FINESSE spectra and the ceilometer backscattering signal as described in
sections 3.1 and 3.2 assuming HBRs and the plate or plate and droxtal small particle contribution. The comparison between the
390   two retrievals is reported in Fig. 15. Overall, the values provided by the FINESSE retrieval and those derived from ceilometer
show agreement within their respective retrieval uncertainties. The ceilometer ODs show a significantly higher uncertainty
because of the noisiness of the ceilometer signal above the CTH, which propagates through the Klett inversion algorithm.
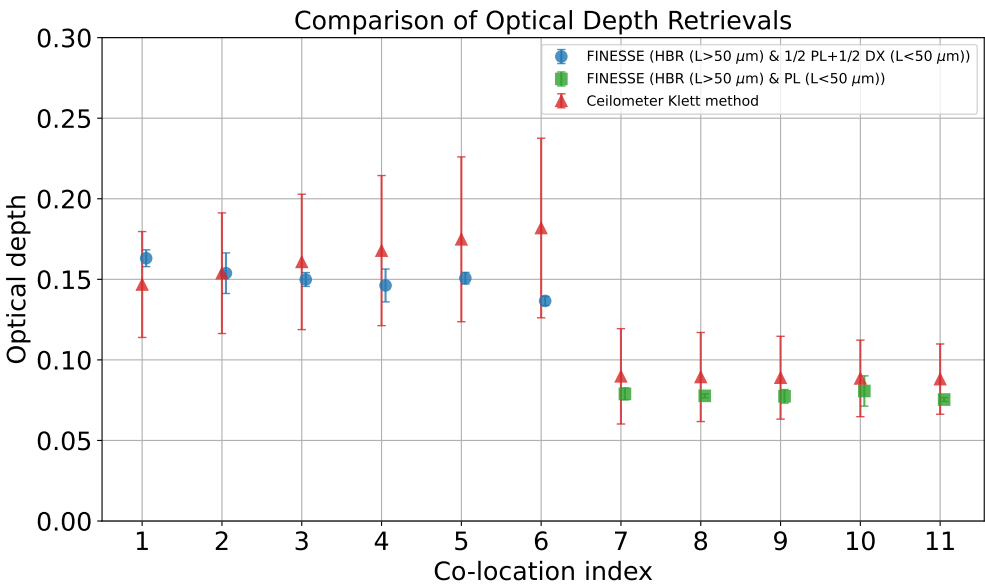

Figure 15. Comparison of the OD retrieved from FINESSE spectra (blue dots and green triangles) and those retrieved from the ceilometer
signal (red triangles) for each scenario.

Despite these uncertainties Fig. 15 clearly shows a distinct thinning of the cirrus between the first six scenarios (centered
around 08:25:30 UTC) and the second five (centered around 08:37:45 UTC). Overall we obtain an average value retrieved
395   from radiometric measurements equal to (0.12±0.01), with the associated error calculated as standard deviation of the mean,
compared with the average value obtained from ceilometer measurements equal to (0.13±0.01), indicating strong consistency
between the retrievals from the different measurements.

The effect of the reduction in OD with time is clearly manifested in the FINESSE spectra as illustrated in Fig. 16, where the
black curve represents the spectrum taken at 08:25:23 UTC and the red curve shows the spectrum measured at 08:37:49 UTC.

400   For these specific spectra the retrieved OD drops from 0.16 to 0.08. The change in OD is most obviously manifested in the atmospheric window with a reduction in both the radiance level and the spectral gradient between 750–1000 cm^{-1}.
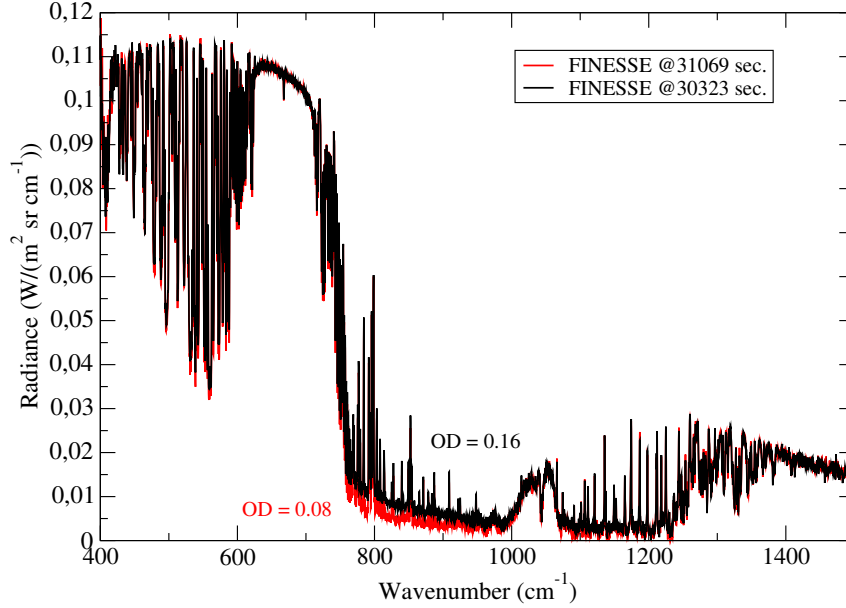
Figure 16. Spectra measured by FINESSE in the presence of cirrus at 30323 and 31069 sec. since midnight (08:25:23 and 08:37:49 UTC) on 17 February 2023. The associated retrieved cirrus optical depths are also provided.

4.3.2   Cirrus effective diameter

Effective diameters retrieved from FINESSE were compared with those obtained from the PSDs provided by the aircraft sensors inside the cirrus. These values were calculated by assuming the four habit distributions introduced in section 3.1.1 and
405   are shown as a function of the co-location index in Fig. 17.

The violet solid lines denote the mean values obtained by averaging the D_{ei} calculated at each altitude using the INCAS KA PSDs. The associated error is calculated as described in section 3.4. Each panel corresponds to the results obtained by assuming a specific habit distribution discussed in section 3.1.2. The red triangles indicate the values retrieved from FINESSE. The assumption of HBRs, either in isolation or mixed with SBRs (top and second panel) clearly show better agreement with
410   the aircraft data than the other assumptions of pure SBRs or a mixture with SCLs (third and bottom panel). In particular, the retrievals obtained when assuming only HBRs show a very good agreement with the aircraft data, with almost all retrieved D_{ei} consistent within uncertainties (top panel). Indeed, over the 11 cases considered, the average retrieved value from the radiometric measurements is (26.5±1.8) μm assuming HBRs which shows good consistency with the average value derived from the in-situ measurements of (31.5±5.0) μm . The calculated standard deviation ($\simeq$10 μm) of the INCAS D_{ei} is also reported
415   in Fig. 4.3.2 along with the corresponding error, showing that all retrieved diameters using the HBR assumption are consistent

with the variability of INCAS retrieved diameter inside the cirrus cloud. The results clearly indicate the strong sensitivity of the FINESSE measurements (and hence retrievals) to the cirrus crystal habit. A preliminary study of the information content suggests that there are no significant differences among the 4 habit distributions and also the maximum differences in corelation between D_{ei}-OD are of the order of 0.2 while the the differences in DOFs of the order of 0.0001. So we deduce that the type of habit distribution, at least among those we have assumed, does not introduce higher degeneracy between cloud parameters and does not affect our capability to retrieve them.

5   Influence of the FIR

In this section we show the importance of information contained within the FIR portion of the spectrum in constraining the cloud property retrievals. Fig. 18 shows the difference in simulated downwelling radiances between the 'best-fit' HBR case and the other three habit choices for cirrus with a D_{ei} of 30 μm and OD of 0.2. The highest sensitivity to crystal shape is seen at wavelengths within the FIR, between 470-600 cm^{-1}. This band is delimited by orange dashed lines in Fig. 18. Moreover, for all three sets of residuals, the differences only exceed the FINESSE NESR between approximately 500-580 cm^{-1}, implying that the radiance fit over this range plays a critical role in determining the retrieved size and optical depth for each habit choice. In essence it is these FIR radiances that allow discrimination between the habits, with the selection of HBR agreeing with the INCAS KA 2D-S and CPI imagery while simultaneously generating ODs and D_{ei}s that show the best match to the INCAS KA PSD observations and ceilometer optical depth retrievals. We would like to emphasize that, based on the FINESSE measurements presented and analyzed, performing the inversion with limited information that excludes the FIR leads to an underestimation of the effective diameter values, but this result cannot, at this time, be generalized to every possible scenario. This clearly calls for a more in-depth investigation, which will be addressed in future work.

Selecting the HBR habit we further investigate the impact of FIR information on the inferred effective diameters. Fig. 19 repeats the information shown in the top panel of Fig. 17 but superposes the equivalent retrievals obtained if only FINESSE radiances over the spectral range 650-1500 cm^{-1}are considered. It is immediately apparent that removing the FIR information results in a poorer fit to the D_{ei} value derived from the INCAS KA observations, particularly during the latter part of the overpass. To explain this behaviour, we investigated three diagnostic indicators, namely the Shannon information content (IC), the number of degrees of freedom (DOFs), and the correlation between the two cloud parameters OD and D_{ei}. The IC is computed as (Rodgers, 2000):

$$\text{IC} = \frac{1}{2} \ln \left| \mathbf{S}_a \mathbf{S}_x^{-1} \right| = \frac{1}{2} \ln \left| (\mathbf{I} - \mathbf{A})^{-1} \right| = \frac{1}{2} \sum_{i=1}^{2} \ln \left(\frac{1}{1 - \lambda_i} \right) \tag{20}$$

where $\mathbf{S}_a$ is the a priori covariance matrix and $\mathbf{S}_x$ is the posterior covariance matrix for the parameters $\mathbf{x} = (D_{ei}, OD)$ and the vertical bars denote the determinant, $\mathbf{A}$ is the averaging kernel matrix, $\mathbf{I}$ is the identity matrix, the vertical bars denote the determinant, and λ_i are the eigenvalues of $\mathbf{A}$. IC and DOFs are evaluated at the first iteration of the retrieval in order to quantify the intrinsic information content of the spectral measurements independently of retrieval convergence effects. The DOFs are
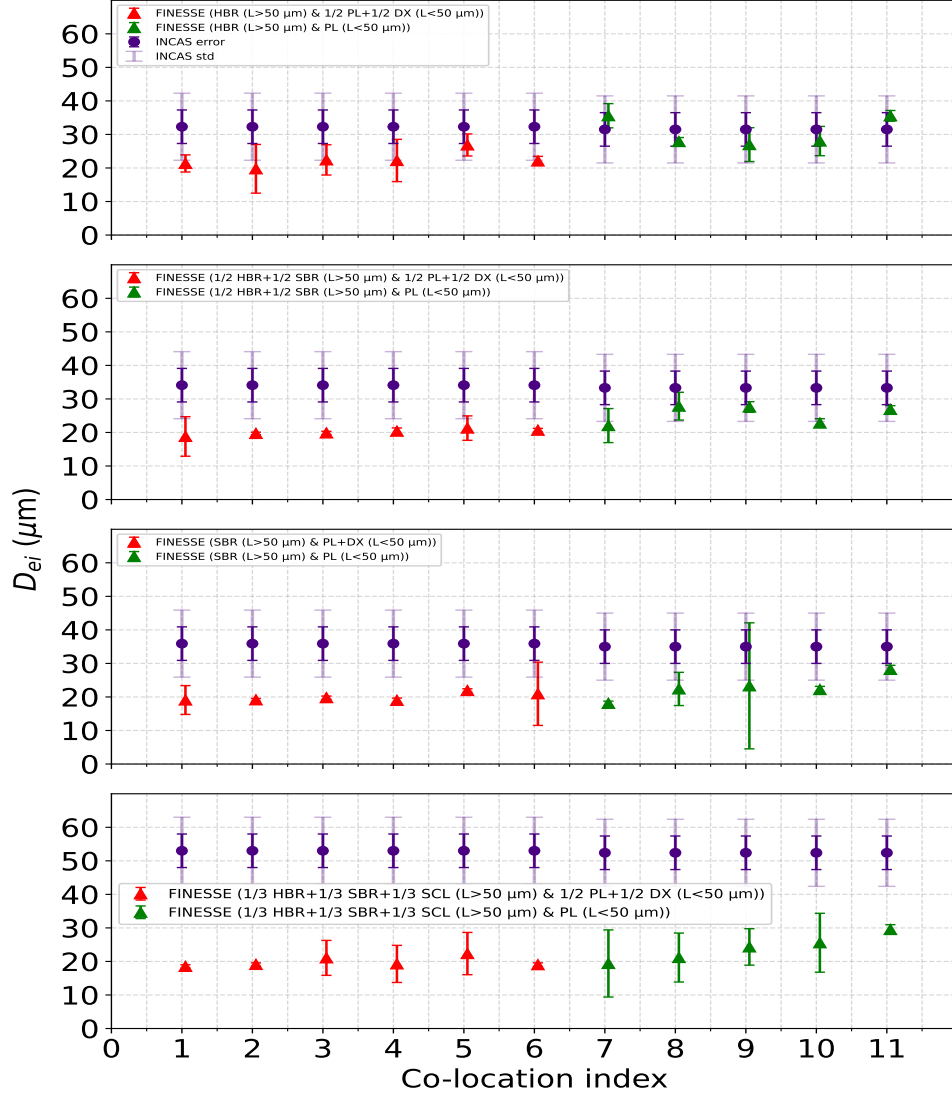
Figure 17. Top panel: comparison of the effective diameters calculated from INCAS KA data (violet dots) with the corresponding error and standard deviaton between 08:19–09:00 UTC on 17 February 2023 and those retrieved from FINESSE (red and green triangles) between 08:25–08:38 UTC of the same day by assuming the habit distribution f_{1h} in Eq. (8). Second panel: same comparison but assuming f_{3h} from Eq. (10). Third panel: same comparison but assuming f_{2h} from Eq. (9). Bottom panel: same comparison but assuming f_{4h} from Eq. (11).

computed as the trace of the averaging kernel matrix restricted to the two cloud parameters:

$$\mathrm{DOF} = \mathrm{tr}(\mathbf{A}) = \sum_{i=1}^{2} \lambda_i \tag{21}$$
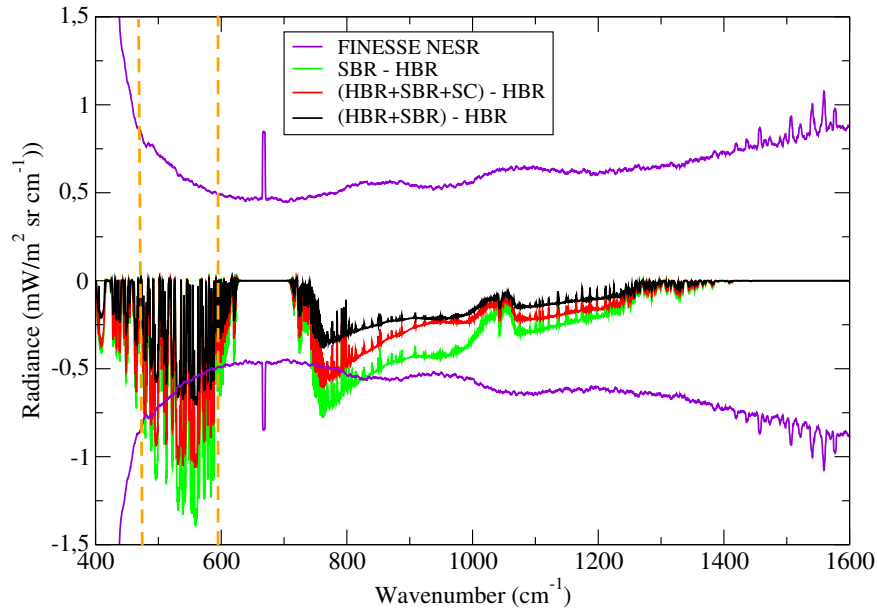
Figure 18. Variations of the simulated spectral radiance by varying the habit distributions used in the analysis of FINESSE measurements (SBR (green), HBR+SBR (black), HBR+SBR+SC (red)) with respect to the case of HBR only. Variations are compared with the FINESSE noise (violet). The band of higher sensitivity to crystal shape in the far-infrared is seen between 470-600 cm^{-1} and is delimited by orange dashed lines. From this spectral band we can discriminate the habit crystal composition.

Although the retrieval algorithm is robust and capable of obtaining the correct solution in synthetic simulations even when the FIR is neglected, the information content in the two cases—with and without FIR—changes significantly, as shown in the upper panel of Fig. 20, where an increase of more than two units is visible when the FIR is considered. Furthermore, we observe an increase in the correlation between the D_{ei}-OD parameters from 0.05 to 0.8, as seen in the middle panel of Fig. 20, meaning that the two parameters become less easily reconstructed independently of each other. The total degrees of freedom for the cloud parameters also decreases when the FIR is not considered (lower panel of Fig. 20). Although the difference in DOFs between the two spectral configurations is small, the corresponding difference in IC is much larger. This is because the inclusion of FIR radiances significantly increases the sensitivity of the measurements to the retrieved parameters, reducing their dependence on the a priori. This effect is evident from the fact that the IC in Eq. 20 is computed as the logarithm of the inverse of (1 minus the eigenvalues of the averaging kernel), so as these eigenvalues approach 1, the IC increases rapidly. Despite the improvement of the retrieval accuracy (the retrieved D_{ei} are more in accordance with the INCAS values), we see a general increase in the statistical retrieval error when the FIR is used. This can be explained by the increase in FINESSE noise over this spectral region (Rodgers, 2000), as visible from Fig. 21.
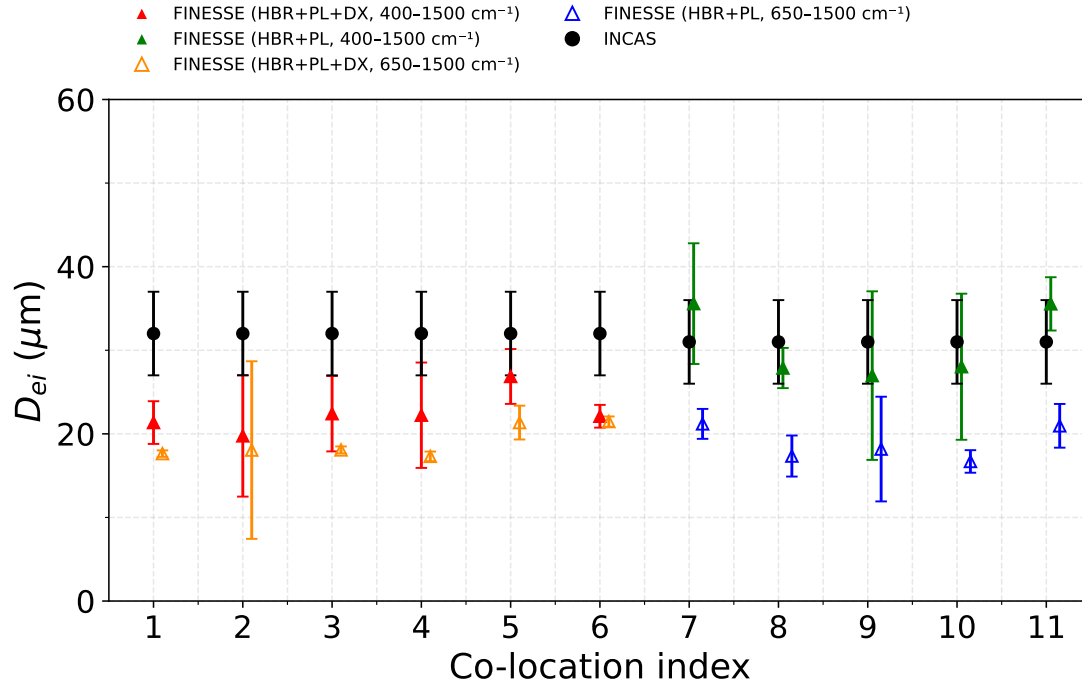
Figure 19. Comparison of the ice effective diameters derived from INCAS KA measurements (black dots) and those retrieved from FINESSE spectra by using the whole spectral band between 400–1500 cm^{-1} (red and green solid triangles) and cutting the FIR portion below 650 cm^{-1} (orange and blue open triangles).

5.1 Discussion

The methodology we chose to validate the scattering properties for ice crystals used in this study is to retrieve all parameters that characterize either the atmosphere or cirrus clouds and then compare the products with the corresponding available mea-
465   surements. In such a way, we avoid over-constraining the atmospheric state we use to simulate the spectral radiance since the available measurements were not perfectly co-located. For example, in this case the HATPRO was located 1.9 km away while the INCAS KA measurements were not instantaneously taken for the entire cirrus vertical profile that FINESSE was measuring but were rather built up over time following the INCAS KA ascent and horizontal sampling. The FINESSE measurements themselves (e.g. Fig. 16) indicate that the cirrus does evolve with time, even over the relatively short period of the INCAS KA
470   observations. To minimise this impact we assume only two parameters from the ancillary measurements: the ice crystal habit inferred from the INCAS KA 2D-S and CPI measurements (hollow bullet rosettes) and the cirrus CTH/CBH derived from ceilometer backscattering profiles. We demonstrate that varying the habit in the simulations and repeating the retrieval proce-
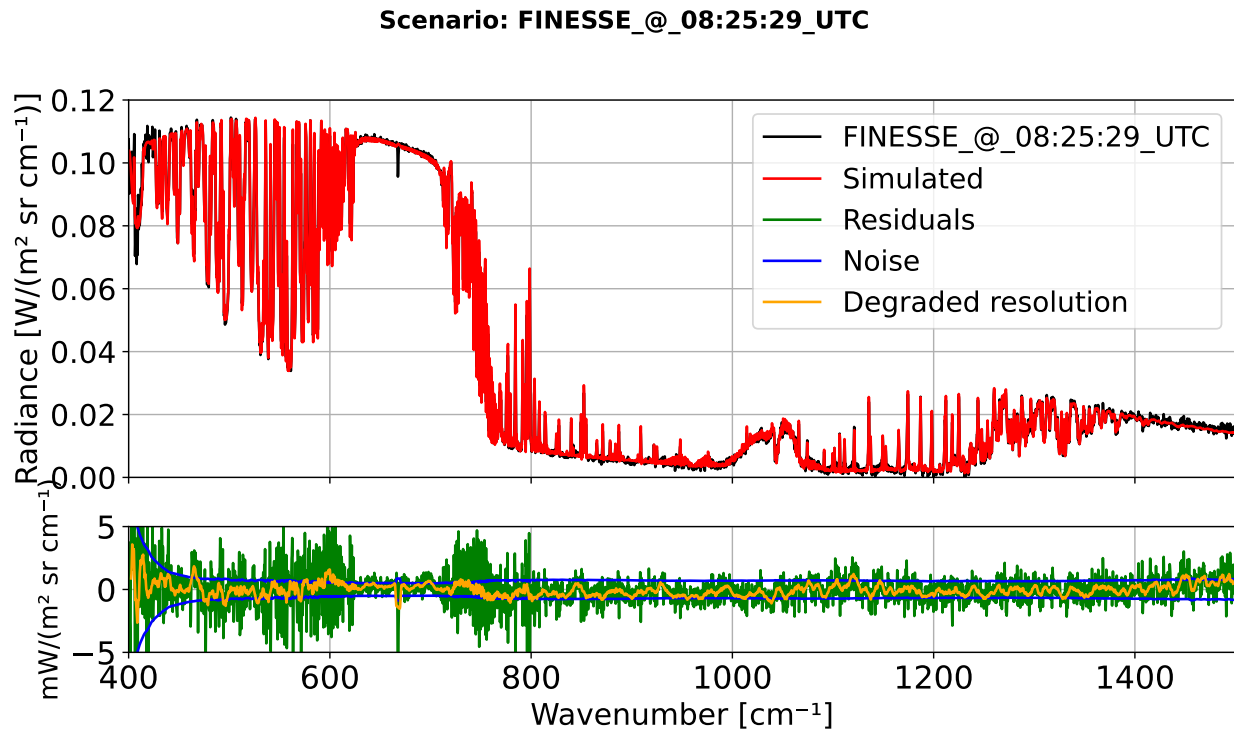
28
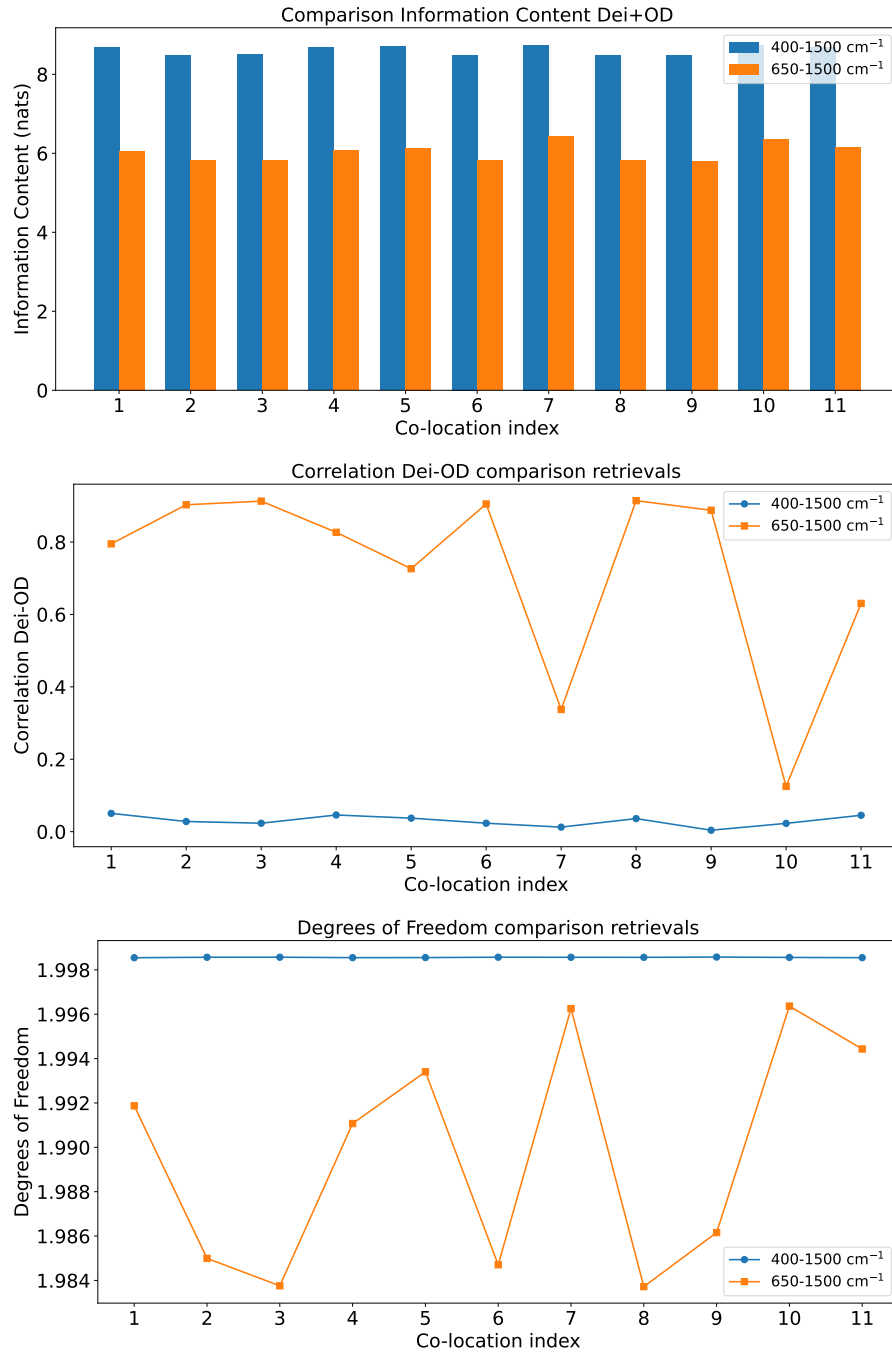
Figure 20. Upper panel: histogram of the information content (IC) after the first retrieval iteration in the full band and cutting the FIR. Middle panel: D_{ei}-OD correlations. Lower panel: cloud degrees of freedom (DOF).

dure results in effective diameters that are not in agreement with the values derived from the PSDs measured by the INCAS KA. This allows us to exclude, for example, the presence of column-like crystals, which indeed appears to be the case from the

475   INCAS KA data.

Scenario: FINESSE_@_08:25:29_UTC

Figure 21. Upper panel: comparison of the simulated spectrum at the last retrieval algorithm iteration (red curve) with the FINESSE measured spectral radiance (black curve) at 30329 sec. since midnight (08:25:29 UTC, scenario 4) on 17 February 2023. Lower panel: the residuals (green curve) are reported in comparison with the noise (blue curves), along with the degraded curve (orange)

Given the caveats noted above, the retrievals from FINESSE show excellent consistency with independent realisations of the atmospheric state and measurements of cirrus properties. They also show the critical importance of the FIR in achieving this consistency. Nonetheless, it is useful to consider the fit of the final retrieved spectra to the observations. As an example, Fig. 21 shows the measured FINESSE spectrum, the simulated radiance at the last iteration, and the associated residuals for scenario

480   4 (08:25:29 UTC, 30329 sec. since midnight) together with their degraded resolution curve. The retrieved D_{ei} and OD were found equal to (22.2±6.3) μm and (0.15±0.01), respectively. For all scenarios the final value of the normalized χ^2_N, the cost function in Eq. (13) divided by the number of spectral channels used, ranged between 2.00–2.10.

Fig. 21 shows that the residuals between the measurement and the simulation predominantly fall within the instrument NESR (blue curves). Notable exceptions are seen within the 667 cm^{-1}CO$_2$ band wings between 550–600 and 750–780 cm^{-1},

485   perhaps because at these wavenumbers, where the spectral lines are very dense, the instrument line shape is not perfectly

characterized. This feature appears systematically for every retrieved spectrum, and is the reason why the χ^2_N is always larger than 2.0. Outside of these regions, in the mid infrared the residuals are very small, indicating that the optical properties are able to correctly reproduce the spectrum. Larger residuals are seen in the FIR region, mostly due to water vapour lines, but also within the 13 main micro-windows discussed by Turner (2005) as shown in Fig. 22: the root mean square (RMS) of the average residuals in radiance are compared with the average noise (calculated by Eq. (22)) in each micro-window.
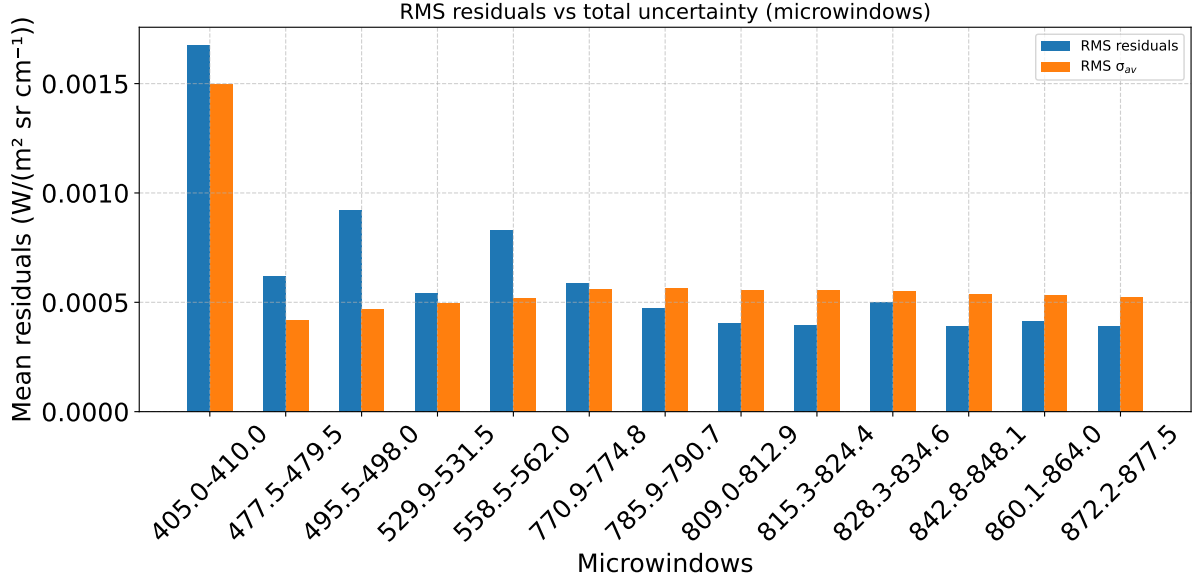
Figure 22. Histogram of the comparison between the root mean square (RMS) of the residuals (blue boxes) and the average noise over all scenarios (orange boxes, calculated Eq. (22)) in the 13 selected microwindows.

$$\sigma_{av} = \sqrt{\frac{\langle \sigma^2_{nesr} \rangle}{N} + \langle \sigma^2_{cal} \rangle} \tag{22}$$

where $N = 11$ number of spectra averaged and the average variance in FINESSE NESR/calibration uncertainty is given by:

$$\langle \sigma^2_{nesr/cal} \rangle = \frac{\sum_i^N \sigma^2_{nesr/cal,i}}{N} \tag{23}$$

The reduced agreement in the FIR region is consistent with previous studies by Bantges et al. (2020), Maestri et al. (2014) and Di Natale et al. (2022).

6 Conclusions

In this paper, we present the first demonstration of consistency between atmospheric measurements and Arctic cirrus cloud parameterizations by combining information from a ground-based spectrometer and sensors, ceilometer, and radiometer with in situ aircraft observations of cloud particle size and habit. Specifically, we make use of spectrally resolved downwelling radiances measured by the Far-INfrarEd Spectrometer for Surface Emissivity (FINESSE), over the range 400–1500 cm^{-1} in conjunction with cloud vertical structure from a ground-based ceilometer and, uniquely, co-located in-situ measurements from a Hawkeye Combination Cloud Particle Probe and a Cloud, Aerosol and Precipitation Spectrometer mounted on the National Institute for Aerospace Research of Romania (INCAS) aircraft. The simultaneous measurements span a period of 13 minutes during the morning of February 17th, 2023.

By applying the Simultaneous Atmospheric and Cloud Retrieval (SACR) code, we are able to simulate the FINESSE spectra and retrieve the cirrus cloud effective diameter (D_{ei}) and visible optical depth (OD), together with the atmospheric temperature and water vapour profile and ozone total column. We selected a subset of 11 spectra between 8:25-8:38 UTC, maximising the overlap with the INCAS aircraft measurements inside the cirrus. Bullet rosettes were identified as the dominant ice crystal habit within the cloud. The PSDs measured at different heights sampled by the aircraft were used to derive the average in-situ D_{ei} for comparison with the values obtained from the FINESSE retrievals. Using the optical properties from Yang et al. (2013) and assuming a Hollow Bullet Rosette (HBR) crystal shape, we obtain agreement between the retrieved D_{ei} and that derived from the aircraft observations within measurement and retrieval uncertainty. Varying the habit distribution, for example, by adding different shapes like hexagonal columns and repeating the retrieval, degrades the agreement.

Observations from the ceilometer allowed us to set the cloud top and bottom height in our simulations and also derive the OD by applying the Klett algorithm. We found a good agreement between the retrieved FINESSE ODs and those derived from the ceilometer for all cases, encompassing when the cirrus was optically thicker, during the first six FINESSE measurements (mean OD = (0.150±0.003)), and thinner during the last five FINESSE measurements (mean OD = (0.077±0.001)).

To complete the analysis, we compared the retrieved water vapour and temperature profiles and ozone total column with co-located values from the ECMWF ReAnalysis-5 (ERA5) database and retrievals from a Humidity and Temperature Profiler (HATPRO) situated at Andøya Space. These comparisons were supplemented, where appropriate, by surface observations from Vaisala probes attached to FINESSE, and by in-cloud temperature measurements from the INCAS aircraft. The retrieved temperature profile above the last fitted level is merely scaled but it turned out to be consistent with the temperatures measured by INCAS probe inside the cirrus and the vertical profile provided by ERA5. At the surface, the level of agreement appeared to show a dependency on the inferred cirrus OD, with FINESSE showing closer agreement to the single ERA5 value during the first six (higher OD) measurements before aligning more closely with the Vaisala values. In all cases the ERA5 and retrieved values were colder than the Vaisala temperatures by up to 1.5 K. A similar low bias was seen between the water vapour volume mixing ratio at the surface obtained from ERA5 and that measured by the Vaisala probe. However, in this case the agreement between the probe and the FINESSE retrieval was much closer. An ERA5 low bias relative to FINESSE was also manifested in the retrievals of the total precipitable water vapour (PWV) above the instrument. In this case, equivalent values derived from

530 the HATPRO support the sense that ERA5 shows a significant humidity underestimate, with PWV retrievals that are closer to those derived from FINESSE, albeit still persistently smaller.

Finally, to understand the importance of information from the far-infrared in determining the cirrus properties we (a) assessed the radiometric sensitivity to the choice of crystal habit and (b) repeated our HBR retrieval but only considered the spectral range 650–1500 cm^{-1}. In common with earlier findings (e.g. Bantges et al. (2020)) the strongest sensitivity to altering the

535 crystal habit is seen in the 500–600 cm^{-1}region. Moreover, even using the HBR habit, when the spectral range is cut to exclude the far-infrared the level of agreement with the aircraft size measurements is significantly reduced. Even though the combination of these two factors suggests the inclusion of the far-infrared is crucial to achieving the improved agreement with the aircraft derived D_{ei} seen for the HBR habit relative to the other habits investigated here, this finding cannot be generalized to every possible scenario. This is primarily because of the limited number of measurements spanning the far-

540 infrared representative of a wider variety of cirrus conditions. However, we hope our findings provide motivation for further measurement campaigns that can address this shortcoming and also be used in support of the future ESA Earth Explorer-9 FORUM mission.

Author contributions. Conceptualization, GDN; Data curation, GDN, JM, ROD, TC, AF, MF, RL, PY; Funding acquisition, HB, HO, DS, LP; Investigation, HB, JM, LW, SP, SM, ROD, TC, SNV, AV, SG, RB, LP; Methodology, GDN; Project administration, HB; Software, GDN

545 ; original draft, GDN; Writing – review & editing, HB, JM, HO. All authors have reviewed and agreed to the published version of the manuscript.

Competing interests. The authors declare that they have no conflict of interest.

References

Bantges, R. J., Brindley, H. E., Murray, J. E., Last, A. E., Russell, J. E., Fox, C., Fox, S., Harlow, C., O'Shea, S. J., Bower, K. N., Baum, B. A., Yang, P., Oetjen, H., and Pickering, J. C.: A test of the ability of current bulk optical models to represent the radiative properties of cirrus cloud across the mid- and far-infrared, Atmospheric Chemistry and Physics, 20, 12 889–12 903, https://doi.org/10.5194/acp-20-12889-2020, 2020.

Baran, A. J.: A review of the light scattering properties of cirrus, J.Quant. Spectrosc. Radit. Transfer, 110, 1239–1260, 2009.

Baran, A. J., Hill, P., Furtado, K., Field, P., and Manners, J.: A Coupled Cloud Physics–Radiation Parameterization of the Bulk Optical Properties of Cirrus and Its Impact on the Met Office Unified Model Global Atmosphere 5.0 Configuration, Journal of Climate, 27, 7725 – 7752, https://doi.org/10.1175/JCLI-D-13-00700.1, 2014.

Bell, B., Hersbach, H., Simmons, A., Berrisford, P., Dahlgren, P., Horányi, A., Muñoz-Sabater, J., Nicolas, J., Radu, R., Schepers, D., Soci, C., Villaume, S., Bidlot, J.-R., Haimberger, L., Woollen, J., Buontempo, C., and Thépaut, J.-N.: The ERA5 global reanalysis: Preliminary extension to 1950, Quarterly Journal of the Royal Meteorological Society, 147, 4186–4227, https://doi.org/https://doi.org/10.1002/qj.4174, 2021.

Belotti, C., Barbara, F., Barucci, M., Bianchini, G., D'Amato, F., Del Bianco, S., Di Natale, G., Gai, M., Montori, A., Pratesi, F., Rettinger, M., Rolf, C., Sussmann, R., Trickl, T., Viciani, S., Vogelmann, H., and Palchetti, L.: The Far-Infrared Radiation Mobile Observation System (FIRMOS) for spectral characterization of the atmospheric emission, Atmospheric Measurement Techniques, 16, 2511–2529, https://doi.org/10.5194/amt-16-2511-2023, 2023.

Bianchini, G., Castagnoli, F., Natale, G. D., and Palchetti, L.: A Fourier transform spectroradiometer for ground-based remote sensing of the atmospheric downwelling long-wave radiance, Atmos. Meas. Tech., 12, 619–635, https://doi.org/doi.org/10.5194/amt-12-619-2019, 2019.

Bony, S., Stevens, B., Coppin, D., Becker, T., Reed, K. A., Voigt, A., and Medeiros, B.: Thermodynamic control of anvil cloud amount, Proceedings of the National Academy of Sciences, 113, 8927–8932, https://doi.org/10.1073/pnas.1601472113, 2016.

Brindley, H. E. and Harries, J. E.: The impact of far i.r. absorption on clear sky greenhouse forcing: sensitivity studies at high spectral resolution, Journal of Quantitative Spectroscopy and Radiative Transfer, 60, 151–180, https://doi.org/https://doi.org/10.1016/S0022-4073(97)00152-0, 1998.

Chepfer, H., Minnis, P., Young, D., Nguyen, L., and Arduini, R. F.: Estimation of cirrus cloud effective ice crystal shapes using visible reflectances from dual-satellite measurements, Journal of Geophysical Research: Atmospheres, 107, AAC 21–1–AAC 21–16, https://doi.org/https://doi.org/10.1029/2000JD000240, 2002.

Choi, Y.-S. and Ho, C.-H.: Radiative effect of cirrus with different optical properties over the tropics in MODIS and CERES observations, Geophysical Research Letters, 33, https://doi.org/https://doi.org/10.1029/2006GL027403, 2006.

Clough, S. A., Shephard, M. W., Mlawer, E. J., Delamere, J. S., Iacono, M. J., Cady-Pereira, K., Boukabara, S., and Brown, P. D.: Atmospheric radiative transfer modeling: a summary of the AER codes, Short Communication, J. Quant. Spectrosc. Radiat. Transfer, 91, 233–244, 2005.

Collins, W. D. and Mlynczak, M. G.: Prospects for measurement of far infrared tropospheric spectra: Implications for climate modeling, in: AGU Fall Meeting Abstracts, vol. 2001, pp. GC32A–0210, 2001.

Cox, C. V., Murray, J. E., Taylor, J. P., Green, P. D., Pickering, J. C., Harries, J. E., and Last, A. E.: Clear-sky far-infrared measurements observed with TAFTS during the EAQUATE campaign, September 2004, Quarterly Journal of the Royal Meteorological Society, 133, 273–283, https://doi.org/https://doi.org/10.1002/qj.159, 2007.

Davis, S. P., Abrams, M. C., and Brault, J. W.: in: Fourier Transform Spectrometry, edited by Davis, S. P., Abrams, M. C., and Brault, J. W., Academic Press, San Diego, ISBN 978-0-12-042510-5, https://doi.org/https://doi.org/10.1016/B978-012042510-5/50009-3, 2001.

600   Dawson, E. and Schiro, K. A.: Tropical High Cloud Feedback Relationships to Climate Sensitivity, Journal of Climate, 38, 583 – 596, https://doi.org/10.1175/JCLI-D-24-0218.1, 2025.

Del Guasta, M.: ICE-CAMERA: a flatbed scanner to study inland Antarctic polar precipitation, Atmospheric Measurement Techniques Discussions, 2022, 1–35, https://doi.org/10.5194/amt-2022-62, 2022.

Del Guasta, M., Morandi, M., Stefanutti, L., Brechet, J., and Piquad, J.: One year of cloud lidar data from Dumont d'Urville (Antarc-

605   tica): 1. General overview of geometrical and optical properties, Journal of Geophysical Research: Atmospheres, 98, 18 575–18 587, https://doi.org/https://doi.org/10.1029/93JD01476, 1993.

Di Natale, G., Palchetti, L., Bianchini, G., and Ridolfi, M.: The two-stream δ-Eddington approximation to simulate the far infrared Earth spectrum for the simultaneous atmospheric and cloud retrieval, Journal of Quantitative Spectroscopy and Radiative Transfer, 246, 106 927, https://doi.org/https://doi.org/10.1016/j.jqsrt.2020.106927, 2020.

610   Di Natale, G., Barucci, M., Belotti, C., Bianchini, G., D'Amato, F., Del Bianco, S., Gai, M., Montori, A., Sussmann, R., Viciani, S., Vogel-mann, H., and Palchetti, L.: Comparison of mid-latitude single- and mixed-phase cloud optical depth from co-located infrared spectrometer and backscatter lidar measurements, Atmospheric Measurement Techniques, 14, 6749–6758, https://doi.org/10.5194/amt-14-6749-2021, 2021.

Di Natale, G., Turner, D. D., Bianchini, G., Del Guasta, M., Palchetti, L., Bracci, A., Baldini, L., Maestri, T., Cossich, W., Martinazzo, M.,

615   and Facheris, L.: Consistency test of precipitating ice cloud retrieval properties obtained from the observations of different instruments operating at Dome C (Antarctica), Atmospheric Measurement Techniques, 15, 7235–7258, https://doi.org/10.5194/amt-15-7235-2022, 2022.

Di Natale, G., Ridolfi, M., and Palchetti, L.: A new approach to crystal habit retrieval from far-infrared spectral radiance measurements, Atmospheric Measurement Techniques, 17, 3171–3186, https://doi.org/10.5194/amt-17-3171-2024, 2024.

620   Dragani, R., Hersbach, H., Simmons, A., and Soci, C.: Preliminary assessement of the ERA5 ozone reanalysis, in: 5th International Conference on Reanalysis (ICR5), pp. 1–15, Rome, Italy, https://doi.org/https://climate.copernicus.eu/sites/default/files/repository/Events/ICR5/Talks/14.Dragani_C3S_ICR5_Nov2017.pdf, 2017.

Elouragini, S.: Useful Algorithms to Derive the Optical Properties of Clouds from a Back-scatter Lidar Return, Journal of Modern Optics,

625   42, 1439–1446, https://doi.org/10.1080/09500349514551261, 1995.

Evans, K. F., Evans, A. H., Nolt, I. G., and Marshall, B. T.: The Prospect for Remote Sensing of Cirrus Clouds with a Submillimeter-Wave Spectrometer, Journal of Applied Meteorology, 38, 514 – 525, https://doi.org/10.1175/1520-0450(1999)038<0514:TPFRSO>2.0.CO;2, 1999.

Field, P. R., Heymsfield, A. J., and Bansemer, A.: Shattering and Particle Interarrival Times Measured by Optical Array Probes in Ice Clouds,

630   Journal of Atmospheric and Oceanic Technology, 23, 1357 – 1371, https://doi.org/10.1175/JTECH1922.1, 2006.

Foth, A.: pyMakeRetrieval, https://doi.org/10.5281/zenodo.13692444, 2024.

Garrett, T. J. and Zhao, C.: Ground-based remote sensing of thin clouds in the Arctic, Atmospheric Measurements and Techniques, 6, 1227–1243, 2013.

Gasparini, B., Mandorli, G., Stubenrauch, C., and Voigt, A.: Basic Physics Predicts Stronger High Cloud Radiative Heating With Warming, Geophysical Research Letters, 51, e2024GL111 228, https://doi.org/https://doi.org/10.1029/2024GL111228, e2024GL111228 2024GL111228, 2024.

Hartmann, D. L. and Larson, K.: An important constraint on tropical cloud - climate feedback, Geophysical Research Letters, 29, 12–1–12–4, https://doi.org/https://doi.org/10.1029/2002GL015835, 2002.

Hersbach, H., Bell, B., Berrisford, P., Hirahara, S., Horányi, A., Muñoz-Sabater, J., Nicolas, J., Peubey, C., Radu, R., Schepers, D., et al.: The ERA5 global reanalysis, Quarterly Journal of the Royal Meteorological Society, 146, 1999–2049, 2020.

Heymsfield, A. J. and Parrish, J. L.: A Computational Technique for Increasing the Effective Sampling Volume of the PMS Two-Dimensional Particle Size Spectrometer, Journal of Applied Meteorology and Climatology, 17, 1566 – 1572, https://doi.org/10.1175/1520-0450(1978)017<1566:ACTFIT>2.0.CO;2, 1978.

Klett, J. D.: Stable analytical inversion solution for processing lidar returns, Appl. Opt., 20, 211–220, https://doi.org/10.1364/AO.20.000211, 1981.

Klett, J. D.: Lidar inversion with variable backscatter/extinction ratios, Appl. Opt., 24, 1638–1643, https://doi.org/10.1364/AO.24.001638, 1985.

Lawson, R. P., Baker, B. A., Schmitt, C. G., and Jensen, T. L.: An overview of microphysical properties of Arctic clouds observed in May and July 1998 during FIRE ACE, Journal of Geophysical Research: Atmospheres, 106, 14 989–15 014, https://doi.org/https://doi.org/10.1029/2000JD900789, 2001.

Lawson, R. P., Baker, B. A., Zmarzly, P., O'Connor, D., Mo, Q., Gayet, J.-F., and Shcherbakov, V.: Microphysical and Optical Properties of Atmospheric Ice Crystals at South Pole Station, Journal of Applied Meteorology and Climatology, 45, 1505–1524, https://doi.org/10.1175/JAM2421.1, 2006.

Lynch, D.: Cirrus clouds: Their role in climate and global change, Acta Astronautica, 38, 859–863, https://doi.org/https://doi.org/10.1016/S0094-5765(96)00098-7, 1996.

Löhnert, U., Turner, D. D., and Crewell, S.: Ground-Based Temperature and Humidity Profiling Using Spectral Infrared and Microwave Observations. Part I: Simulated Retrieval Performance in Clear-Sky Conditions, Journal of Applied Meteorology and Climatology, 48, 1017 – 1032, https://doi.org/10.1175/2008JAMC2060.1, 2009.

Maesh, A., Walden, V. P., and Warren, S. G.: Ground-Based Infrared Remote Sensing of Cloud Properties over the Antarctic Plateau. Part I: Cloud-Base Heights, Journal of Applied Meteorology, 40, 1265–1277, 2001a.

Maesh, A., Walden, V. P., and Warren, S. G.: Ground-based remote sensing of cloud properties over the Antarctic Plateau: Part II: cloud optical depth and particle sizes, Journal of Applied Meteorology, 40, 1279–1294, 2001b.

Maestri, T., Rizzi, R., Tosi, E., Veglio, P., Palchetti, L., Bianchini, G., Girolamo, P. D., Masiello, G., Serio, C., and Summa, D.: Analysis of cirrus cloud spectral signatures in the far infrared, Journal of Geophysical Research, 141, 49–64, 2014.

Marquardt, D. W.: An algorithm for least-squares estimation of non-linear parameters, SIAM J. Appl. Math., 11, 431–441, 1963.

Meyer, K., Platnick, S., Arnold, G. T., Holz, R. E., Veglio, P., Yorks, J., and Wang, C.: Cirrus cloud optical and microphysical property retrievals from eMAS during SEAC[4]RS using bi-spectral reflectance measurements within the 1.88 µm water vapor absorption band, Atmospheric Measurement Techniques, 9, 1743–1753, https://doi.org/10.5194/amt-9-1743-2016, 2016.

Murray, J. E., Warwick, L., Brindley, H., Last, A., Quigley, P., Rochester, A., Dewar, A., and Cummins, D.: The Far INfrarEd Spectrometer for Surface Emissivity (FINESSE). Part 1: Instrument description and level 1 radiances, Atmospheric Measurement Techniques Discussions, 2024, 1–32, https://doi.org/10.5194/amt-2024-22, 2024.

Palchetti, L., Bianchini, G., Natale, G. D., and Guasta, M. D.: Far-Infrared radiative properties of water vapor and clouds in Antarctica, B. Am. Meteorol. Soc., 96, 1505–1518, https://doi.org/10.1175/BAMS-D-13-00286.1, 2015.

Palchetti, L., Natale, G. D., and Bianchini, G.: Remote sensing of cirrus microphysical properties using spectral measurements over the full range of their thermal emission, J. Geophys. Res., 121, 1–16, https://doi.org/10.1002/2016JD025162, 2016.

Palchetti, L., Brindley, H., Bantges, R., Buehler, S. A., Camy-Peyret, C., Carli, B., Cortesi, U., Del Bianco, S., Di Natale, G., Dinelli, B. M., Feldman, D., Huang, X. L., C.-Labonnote, L., Libois, Q., Maestri, T., Mlynczak, M. G., Murray, J. E., Oetjen, H., Ridolfi, M., Riese, M., Russell, J., Saunders, R., and Serio, C.: FORUM: unique far-infrared satellite observations to better understand how Earth radiates energy to space, Bulletin of the American Meteorological Society, pp. 1–52, https://doi.org/10.1175/BAMS-D-19-0322.1, 2020.

Platnick, S., Meyer, K. G., King, M. D., Wind, G., Amarasinghe, N., Marchant, B., Arnold, G. T., Zhang, Z., Hubanks, P. A., Holz, R. E., Yang, P., Ridgway, W. L., and Riedi, J.: The MODIS Cloud Optical and Microphysical Products: Collection 6 Updates and Examples From Terra and Aqua, IEEE Transactions on Geoscience and Remote Sensing, 55, 502–525, https://doi.org/10.1109/TGRS.2016.2610522, 2017.

Raghuraman, S. P., Medeiros, B., and Gettelman, A.: Observational Quantification of Tropical High Cloud Changes and Feedbacks, Journal of Geophysical Research: Atmospheres, 129, e2023JD039 364, https://doi.org/https://doi.org/10.1029/2023JD039364, e2023JD039364 2023JD039364, 2024.

Remedios, J. J., Leigh, R. J., Waterfall, A. M., Moore, D. P., Sembhi, H., Parkes, I., Greenhough, J., Chipperfield, M. P., and Hauglustaine, D.: MIPAS reference atmospheres and comparisons to V4.61/V4.62 MIPAS level 2 geophysical data sets, Atmospheric Chemistry and Physics Discussions, 7, 9973–10 017, https://doi.org/10.5194/acpd-7-9973-2007, 2007.

Rodgers, C. D.: Inverse methods for atmospheric sounding : theory and practice, World Scientific Publishing, 2000.

Shupe, M. D., Turner, D. D., Walden, V. P., Bennartz, R., Cadeddu, M. P., Castellani, B. B., Cox, C. J., Hudak, D. R., Kulie, M. S., Miller, N. B., Neely, R. R., Neff, W. D., and Rowe, P. M.: High and Dry: New Observations of Tropospheric and Cloud Properties above the Greenland Ice Sheet, Bulletin of the American Meteorological Society, 94, 169 – 186, https://doi.org/10.1175/BAMS-D-11-00249.1, 2013.

Stackhouse, P. W. and Stephens, G. L.: A Theoretical and Observational Study of the Radiative Properties of Cirrus: Results from FIRE 1986, Journal of Atmospheric Sciences, 48, 2044 – 2059, https://doi.org/10.1175/1520-0469(1991)048<2044:ATAOSO>2.0.CO;2, 1991.

Stephens, G. L., Tsay, S.-C., Stackhouse, P. W., and Flatau, P. J.: The Relevance of the Microphysical and Radiative Properties of Cirrus Clouds to Climate and Climatic Feedback, Journal of Atmospheric Sciences, 47, 1742 – 1754, https://doi.org/10.1175/1520-0469(1990)047<1742:TROTMA>2.0.CO;2, 1990.

Turner, D. D.: Arctic mixed-Phase cloud properties from AERI lidar observation: algorithm and results from SHEBA, Journal of Applied Meteorology, 44, 427–444, 2005.

Turner, D. D. and Mlawer, E. J.: The Radiative Heating in Underexplored Bands Campaigns, Bulletin of the American Meteorological Society, 91, 911 – 924, https://doi.org/10.1175/2010BAMS2904.1, 2010.

Turner, D. D., Ackerman, S. A., Baum, B. A., Revercomb, H. E., and Yang, P.: Cloud Phase Determination Using Ground-Based AERI Observations at SHEBA, Journal of Applied Meteorology, 42, 701–715, 2003.

Vâjâiac, S. N., Calcan, A., David, R. O., Moacă, D.-E., Iorga, G., Storelvmo, T., Vulturescu, V., and Filip, V.: Post-flight analysis of detailed size distributions of warm cloud droplets, as determined in situ by cloud and aerosol spectrometers, Atmospheric Measurement Techniques, 14, 6777–6794, https://doi.org/10.5194/amt-14-6777-2021, 2021.

Walbröl, A., Susanne, C., Ronny, E., Emiliano, O., Hannes, G., Martin, R., Julian, H., Dietrich, A., Marion, M., and Kerstin, E.: Atmospheric temperature, water vapour and liquid water path from two microwave radiometers during MOSAiC, Scientific Data, 9, https://doi.org/10.1038/s41597-022-01504-1, 2022.

Woods, S., Lawson, R. P., Jensen, E., Bui, T. P., Thornberry, T., Rollins, A., Pfister, L., and Avery, M.: Microphysical Properties of Tropical Tropopause Layer Cirrus, Journal of Geophysical Research: Atmospheres, 123, 6053–6069, https://doi.org/https://doi.org/10.1029/2017JD028068, 2018.

Wu, W. and McFarquhar, G. M.: On the Impacts of Different Definitions of Maximum Dimension for Nonspherical Particles Recorded by 2D Imaging Probes, Journal of Atmospheric and Oceanic Technology, 33, 1057 – 1072, https://doi.org/10.1175/JTECH-D-15-0177.1, 2016.

Yang, P., Huang, W. H., Baum, H.-L., Hu, B. A., Kattawar, Y. X., Mishchenko, G. W., I., M., and Fu, Q.: Scattering and absorption property database for nonspherical ice particles in the near-through far-infrared spectral region, Appl. Optics, 44, 5512–5523, 2005.

Yang, P., Bi, L., Baum, B. A., Liou, K.-N., Kattawar, G. W., Mishchenko, M. I., and Cole, B.: Spectrally Consistent Scattering, Absorption, and Polarization Properties of Atmospheric Ice Crystals at Wavelengths from 0.2 to 100 μm, Journal of atmospheric sciences, 70, 330–347, 2013.

Yang, P., Liou, K.-N., Bi, L., Liu, C., Yi, B., and Baum, B. A.: On the radiative properties of ice clouds: Light scattering, remote sensing, and radiation parameterization, Advances in Atmospheric Sciences, 32, 2127–2135, https://doi.org/10.1007/s00376-014-0011-z, 2015.

Zhou, C., Dessler, A. E., Zelinka, M. D., Yang, P., and Wang, T.: Cirrus feedback on interannual climate fluctuations, Geophysical Research Letters, 41, 9166–9173, https://doi.org/https://doi.org/10.1002/2014GL062095, 2014.